NUMERICAL STUDY OF MECHANICAL PROPERTIES OF HYBRID SOLAR CELL THIN FILM LAYERS BY NANOINDENTATION

A Thesis Submitted to the Department of Materials Science and Engineering at
African University of Science and Technology
In Partial Fulfilment of the Requirements for the Degree of

MASTER OF SCIENCE

In The Department of Materials Science And Engineering

BY

AJAH, JAMAEL CHIMA

Abuja, Nigeria

SUPERVISED BY:

DR. ANYE VITALIS

June, 2021

CERTIFICATION

This is to certify that the thesis titled “Numerical study of mechanical properties of hybrid solar cells thin film layers by nanoindentation” submitted to the school of postgraduate studies, African University of Science and Technology (AUST), Abuja, Nigeria for the award of the Master's degree is a record of original research carried out by Jamael Chima Ajah in the Department of Materials Science and Engineering.

NUMERICAL STUDY OF MECHANICAL PROPERTIES OF HYBRID SOLAR CELL THIN FILM LAYERS BY NANOINDENTATION

By

Jamael Chima Ajah

A THESIS APPROVED BY THE DEPARTMENT OF MATERIALS SCIENCE AND ENGINEERING

RECOMMENDED: _____

Supervisor, Dr. Vitalis Anye

_____

Prof. Peter Azikiwe Onwualu

Head, Department of Materials Science and Technology

APPROVED: _____

Chief Academic Officer

_____

ABSTRACT

The evolution in the use of solar panels for generation of electricity has been immense throughout the world, especially in the last decade. This has seen both organic and inorganic solar panels, with both of them possessing unique mechanical properties. In recent years, however, research has been focused on the attempt to improve the use of organic and hybrid solar cells, as these are relatively cheaper than the inorganic ones. The major challenge is in its stability and mechanical properties, as it has restricted its use to the laboratory. The mechanical properties can be gotten through experimental method and through Finite Element Analysis (FEA). This project therefore sought to use FEA investigate the mechanical properties of a layer of hybrid solar cells thing film by nanoindentation. The set-up of the active layers of the perovskite, FTO-coated glass and Methyl Ammonia Lead Iodide was created on Abaqus 6.14 software, boundary conditions, constraints and appropriate meshing was done and similar mechanical properties were inputted using a 2D axis-symmetric model for the indentation. The results obtained where then further analysed to obtain mechanical properties such as Elastic Modulus and Hardness. It demonstrates that FEA can be effectively used to study the mechanical properties of both individual layers of a hybrid solar cell and the whole setup.

Keywords: Solar-Cell, Perovskite, Nanoindentation, Finite Element Analysis

I dedicate this thesis to my late uncle, Uncle Magnus Onuabuchi Ajah, who passed on the 7th of May, 2020 during the course of my master's program. A dear uncle who was ever present for my family in all times. Uncle, we will continue to make progress in all our endeavours.

ACKNOWLEDGEMENT

First, I wish to thank the almighty God, the maker of heaven and the earth for his love, guidance and protection upon me throughout the period of my stay in AUST. He has been great, despite my unfaithfulness. I pledge to remain ever loyal and faithful to him.

Next, I will thank my wonderful family, my father, Mr. Michael O. Ajah, a dear father, one who sacrificed all for me, his Mojishola. As I have grown, I see that I am reflection of him, day by day. I love you sir. My own *mama na*, Mrs. Cecilia O. Ajah, a special woman, who despite her health challenges has risen up early every day to prepare for the home, who still calls me, her bobo, and leaves food for me to eat. I love you to the moon and back, mama. I will thank my siblings, Pharm. Uchechi Umeh, who got married and gave birth to my wonderful nephew, Ugonnaya, while I was still in AUST. My younger brother, Eliezer, La Grangea Ajah, my *mannest* man and closest friend. My baby, Grace E. Ajah, who made my learning process during the lockdown wonderful. I was a special beneficiary of all her wonderful and amazing culinary skills. I love you all.

I will thank my Supervisor, Dr. Anye Vitalis, a great man, excellent teacher, whose understanding of Mathematics and Science is unrivalled in the department. I appreciate the wealth of knowledge you have impacted on me in me stay in AUST. Your guidance throughout the project was awesome. I also really appreciate your patience and understanding despite my lapses in carrying out the project. Thank you, sir. Congratulations to your baby girl, born during my program in AUST. I thank all other faculties, from the HOD, Prof. Peter. A. Onwualu, a father and a mentor, Prof. Wole Soboyejo, a man I look up to, Dr. Shola Odusanya, an amazing scholar, Dr. Bello Hakeem, a researcher per excellence, Dr. Emmanuel Boakye, the ceramics Czar. I will thank Dr. Ma’aruf, a great mathematician who I bonded well with, Dr. Rajesh

Prasad, and amazing personality, one with outstanding intellectual ability and humour. Finally, I will really thank Professor Douglas Buttrey, one who opened my eyes to the beuty of thermodynamics and has really been instrumental in my journey after AUST. I will not disappoint you, sir.

To the rest of my colleagues, I appreciate you all, especially my co-supervisees, Nalyanya Fredrick and Apam Francis Akudago. More wins.

TABLE OF CONTENTS

LIST OF FIGURES

LIST OF TABLES

CHAPTER ONE

1.0 BACKGROUND

Globally, there has been a great drive towards the shift from conventional sources of energy to alternative sources of energy, which are cleaner and better. This is because, although the conventional sources of energy are quite reliable, steady and have stood the test of time, its carbon emission, occasioned by the use of fossil fuels has adversely affected the climate. This climate change results in harsher environmental conditions, as was the case in the 5-day power outage in Texas, due to freezing of power grids (Storrow, 2021) and even the harsher and inconsistent weather in Nigeria (Ritvo, 2018). In a bid to move towards these cleaner sources of energy, attention has been focused on geothermal systems (Carlino et al., 2012), wind (Leung & Yang, 2012), hydrogen fuel (Karmakar et al., 2012) and solar energy (Righini & Enrichi, 2020).

The amount of energy available from the sun is sufficient to power the planet for a very long time (Righini & Enrichi, 2020). This energy is transformed from the light energy of the sun to electricity through the use of devices called photovoltaics. Much advances have been made in the selection, processing, properties and performance of these photovoltaics for the past several years (Rashel et al., 2017). From the use of inorganic materials, like silicon wafer, to the use of organic and hybrid materials (perovskites), engineering and scientific research has led to outstanding progress in the area of photovoltaics. Photovoltaics, however, have not fully replaced conventional sources of energy because, although the use of these materials as alternative sources of energy seems very feasible, the cost of usage, when compared with conventional sources of energy is very high, especially in cases of inorganic photovoltaics, where silicon wafers are used. Organics materials clearly overcome this challenge of higher relative cost; however, it is not without its own challenges, majorly stability, relatively poor

opto-electronic properties and lower mechanical properties. This has hindered its progression from synthesis in the laboratory to large scale production for industrial use (Lipomi, 2018). In an attempt to optimize these challenges, hybrid photovoltaics, especially perovskites, have found great interest, and use, where organic and inorganic materials are combined so that desirable properties of both are utilized, organic materials for its relative low cost and high through put, and inorganic materials for its tuneability in absorption spectra. These hybrid solar cells have the potentials to achieve high power conversion efficiency (PCE). Some challenge that it faces are due to its mechanical properties, especially at the relevant interface. A way to address this challenge is in carrying out research on the mechanical properties of these hybrid photovoltaics, both as a complete system and on each of their respective layers, in order to understand the dynamics on both the bulk materials and on a nanoscale. This approach gives provides better insight as scientist and engineers seek to improve this photovoltaics. One technique used for this is nanoindentation.

Nanoindentation is a non-destructive technique used for the characterization of mechanical response of materials. It makes use of an indenter whose penetration depth is in the order of magnitude of nanometers, usually 200 nm (based in ISO 14577-1) (Khan et al., 2018). This makes it the best technique used in the measurement of mechanical properties of thin films that are in the nanoscale. As with many mechanical testing methods, nanoindentation can be simulated through the process called Finite Element Analysis (FEA). FEA gives insight into what happens at the thin films, which may not easily be obtained through experiments (Ivankov et al., 2013). Finite element Analysis or Finite Element Method (FEM) is usually used to investigate complex stress and strain fields under the indenter tip, which can be extremely difficult to achieve under experiments). It is also relevant to be used when experimental

nanoindentation shows limitations. Multiple works have been done in the area of FEA using nanoindentation on bulk materials and different kinds of thin films. This has been used to investigate effects of pile-up or sink-in, substrate effect and effect of thickness of films on different materials (Chen & Vlassak, 2001; Pelegri & Huang, 2008). This work looks to specifically analyze what happens at the interface of the nano indenter and the active layer of hybrid photovoltaics. Mechanical properties that this work is interested in include: hardness, elastic modulus, endurance loads and various parameters like optimal critical load, thickness and stress distribution between the substrate (FTO coated glass) and the thin active layer (MAHPPV).

1.2 AIM AND OBJECTIVES

This work is aimed at conducting a FEM study of the mechanical properties of the thin film photovoltaics.

It will be achieved through the following:

- Obtaining mechanical properties of the component parts of the setup from literature
- Creating a 2-D axisymmetric model of the indenter and the layered material with appropriate dimensions
- Creating constraints and boundary load condition for the set up.
- Creating a fine mesh and carrying out the indentation process.
- Varying parameters like loading conditions, and layer conditions
- Analysing the obtained data and making conclusions.

1.3 PROBLEM STATEMENT

Photovoltaics are multilayer devices, with each of the layers performing specified functions. The layer where the actual conversion of light energy to electricity takes place is called the active layer. In perovskite solar cells, this is where the perovskite material stays. The mechanical properties of this layer have not been fully investigated. The mechanical properties of these thin films are of immense importance as under service life, these films may fail, resulting in loss of the system as a whole. It is therefore expedient to study these properties in the nanoscale, identify issues and resolve same as such scale, rather than a top to bottom approach which may be catastrophic in nature.

1.4 SCOPE AND OUTLINE OF THESIS

Although the complete setup of the solar panel is of relevant in practical applications, the scope of this project is limited to thin films, (specifically the substrate and active layers). Also, the type of hybrid solar cell that will be studied is perovskite thin films. Thin films are currently being used in every engineering field, due to its ability to improve mechanical properties of bulk materials. Furthermore, the work will be restricted to using FEM of nanoindentation to study this effects, especially critical load to failure and load that may cause disintegration of the materials using a two-dimensional axis-symmetric model. This is because, the results of a 2-D model give actual credence to experimental work.

After the detailed introduction given in chapter one, a thorough and specific literature review is presented in chapter two. In chapter 3, the methods used, first in experiments and for the simulation is presented. The tests carried out and the result and interpretation of them are shown in chapter four of this work, while chapter 5 presents the conclusion drawn and subsequent recommendations for future work.

1.5 REFERNCES

Benjamin Storrow, (2021) E&E News, https://www.scientificamerican.com/article/why-the-deep-freeze- caused-texas-to-lose-power/

Carlino, S., Somma, R., Troise, C., & De Natale, G. (2012). The geothermal exploration of Campanian volcanoes: Historical review and future development. In *Renewable and Sustainable Energy Reviews* (Vol. 16, Issue 1, pp. 1004–1030). https://doi.org/10.1016/j.rser.2011.09.023

Chen, X., & Vlassak, J. J. (2001). Numerical study on the measurement of thin film mechanical properties by means of nanoindentation. *Journal of Materials Research*, *16*(10), 2974–2982. https://doi.org/10.1557/JMR.2001.0408

Dennis Y.C. Leung, Yuan Yang, Wind energy development and its environmental impact: A review, *Renewable and Sustainable Energy Reviews*, Volume 16, Issue 1, 2012,

Iankov, R., Datcheva, M., Cherneva, S., & Stoychev, D. (2013). Finite element simulation of nanoindentation process. *Lecture Notes in Computer Science (Including Subseries Lecture Notes in Artificial Intelligence and Lecture Notes in Bioinformatics)*, *8236 LNCS*, 319–326. https://doi.org/10.1007/978-3-642-41515-9_35

Karmakar, A., Karmakar, S., & Mukherjee, S. (2012). Biodiesel production from neem towards feedstock diversification: Indian perspective. In *Renewable and Sustainable Energy Reviews* (Vol. 16, Issue 1, pp. 1050–1060). https://doi.org/10.1016/j.rser.2011.10.001

Khan, M. I., Shakoor, A., Azam, K., Habib, M., Muhammad, R., Shah, S. A., & Khan, A. (2018). Experimental and numerical analysis of nanoindentation of Ti-6246 alloy. *Particulate Science and Technology*, *36*(4), 408–418. https://doi.org/10.1080/02726351.2016.1267287

Leung, D. Y. C., & Yang, Y. (2012). Wind energy development and its environmental impact: A review. In *Renewable and Sustainable Energy Reviews* (Vol. 16, Issue 1, pp. 1031–1039). Pergamon. https://doi.org/10.1016/j.rser.2011.09.024

Lipomi, D. J. (2018). Organic Photovoltaics: Focus on Its Strengths. *Joule*, *2*(2), 195–198. https://doi.org/10.1016/j.joule.2017.12.011

Pelegri, A. A., & Huang, X. (2008). Nanoindentation on soft film/hard substrate and hard film/soft substrate material systems with finite element analysis. *Composites Science and Technology*, *68*(1), 147–155. https://doi.org/10.1016/j.compscitech.2007.05.033

Rashel, M. R., Goncalves, T., Tlemcani, M., & Melicio, R. (2017). *Photovoltaic cell performance analysis under different ambient temperature and wind speed for sustainable energy*. *January*.

Righini, Giancarlo & Enrichi, Francesco. (2020). Solar cells' evolution and perspectives: a short review. 10.1016/B978-0-08-102762-2.00001-X.

CHAPTER TWO

2.0 LITERATURE REVIEW

2.1 PHOTOVOLTAICS

Photovoltaics (PV) are devices that work with the principle of conversion of electricity through light. It has also become a viable alternative (clean energy resources) for conventional sources of energy (fossil fuels). Most of the commercially available PV devices currently in use are the silicon-based devices. This is due to its peculiar properties and relative higher advantage of long lifetime, sustainability, availability and non-toxicity (Donne et al., 2013). Although the cost of production of silicon-based PV devices has seen a gradual decline, it is still relatively higher than fossil fuel-based energy. Alternative PV devices that research has focused on include thin film devices, organic solar cells and hybrid solar cells, especially, perovskites. This has seen a form of progression, from first generation of silicon wafers to second generation solar cells centred on thin films and third generation solar cells that work on donor-acceptor interfaces. Examples of third-generation photovoltaics include organic solar cells, quantum dot solar cells and perovskites.

2.1.1 PEROVSKITE SOLAR CELLS

The meaning of the name, “perovskite” was about the discovery of the crystal structure of calcium titanate in 1839 by the German mineralogist Gustave Rose. Its origin was named after the Russian mineralogist Lev Perovski (Zhengqi & Ahalapitaya 2018). It is now used to refer to all compound with the same crystal structure as calcium titanate. Its light absorption layer has the

general formula of ABX_3, where A is an organic cation (methylammonium, CH_3NH_3*, MA* or formamidinium $CH(NH_2)_2$*, FA*), B is a metal cation (Pb^{2+}, Sn^{2+}) and X stands for the halide anion (Cl^-, Br^-, or I^- or o coexistence of several halogens).

The interest in perovskite materials is due to its cubic lattice-nested octahedral layered structure and its peculiar thermal, opto-electronic and electromagnetic properties.(Zhou et al., 2018). This structure confers on perovskites excellent characteristic. It has a large dielectric constant for transmission and collection of electrons and holes, making it possible for electrons and holes to be transmitted simultaneously with the transmission distance up to 1μm. (Green et al., 2014). Perovskites, as light-absorbing layers can absorb energy efficiently. (Stoumpos et al., 2013)

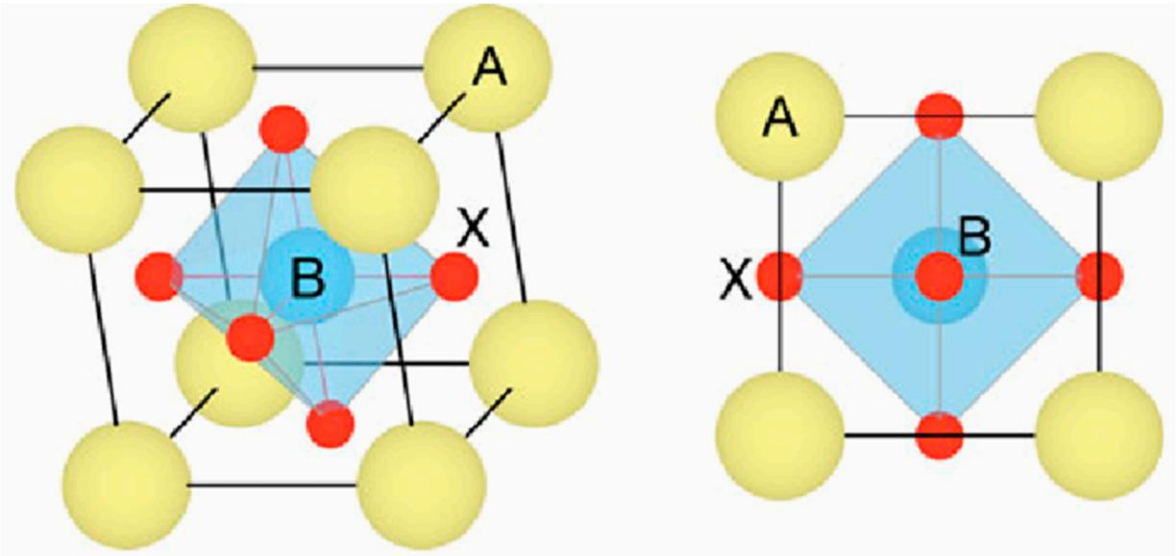

Figure 2.1: Typical perovskite cubic lattice of the form ABX_3 (Zhengqi & Ahalapitaya 2018; Jain et al., 2013)

As with most materials with regular crystal structure, phases of perovskite materials change with change in temperature. At temperatures below 100K, it displays stable orthorhombic (gamma) phase. Kawamura et al., (2002) first showed that when the temperature increased to 160K, the

tetragonal (beta phase) started to appear to replace the original orthorhombic (gamma) phase. The tetragonal (beta) phase changes to another stable cubic (alpha) phase (Whitfield et al., 2016). These crystal structtures are displayed in Figure 2 below. For thermal stability at higher temperatures, the tetragonal-cubic phase transition at higher temperatures has some influence on the thermal stability of perovskite materials.

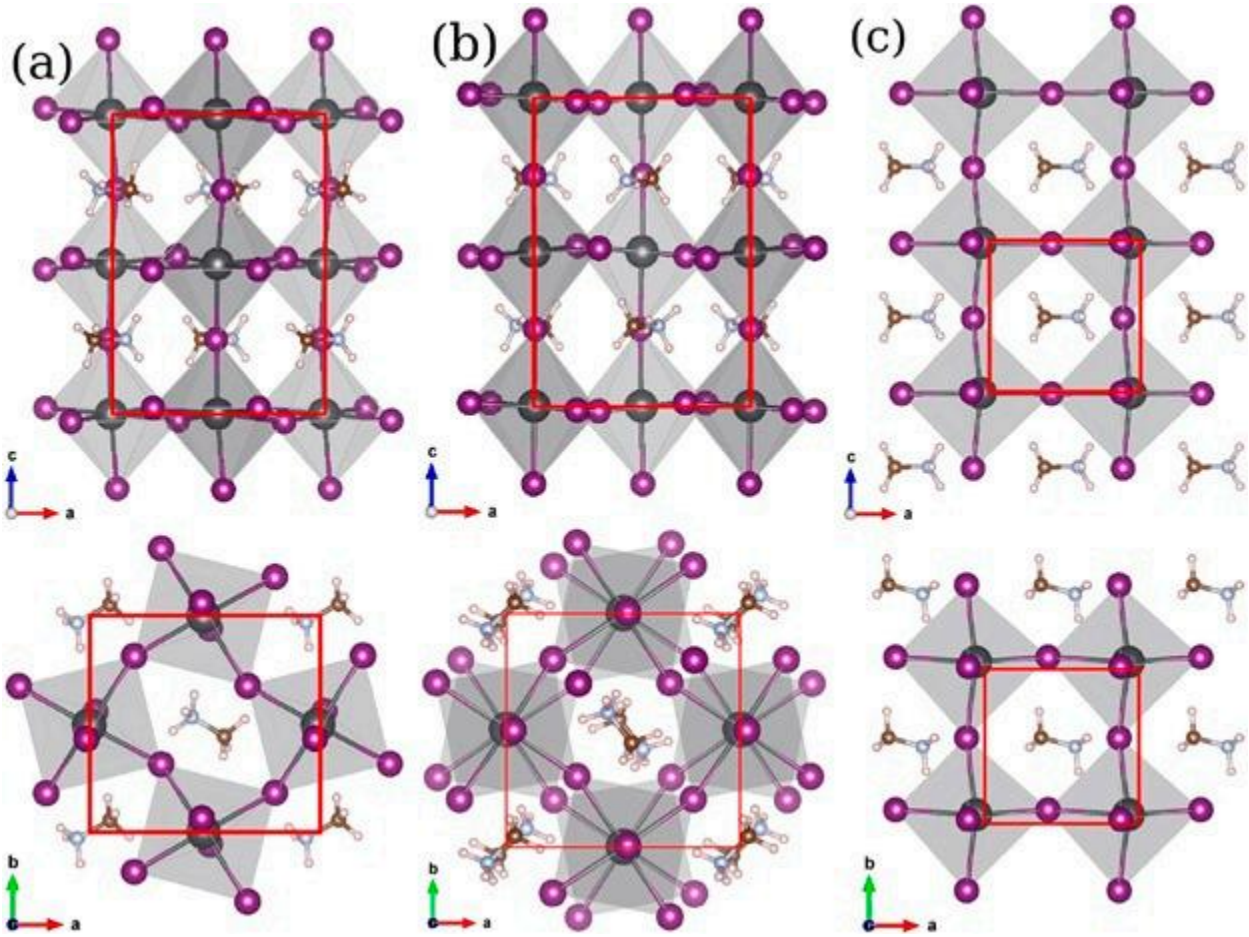

Figure 2.2. Comparison of (a) orthorhombic; (b) tetragonal and (c) cubic perovskite phases obtained from structural optimization of MAPbI3. Top row: a-c-plane and bottom row: a-b-plane (Korshunova et al., 2016)

2.1.2 STUCTURE AND WORKING PRINCIPLES OF PEROVKITES

There are two main structure of perovskite solar cells that have been developed in recent times. These are the mesoscopic architecture and the planar heterojunction structure.

Mesoporous Structure: These have high porosity and large specific area of up to 1000 m^2/g. It allows the perovskite absorber to adhere to mesoporous metal oxide framework, which helps it increase the light-receiving area of the photosensitive material.

Zhou et al., (2018) puts it clearly in the review article on PSCs: "typical mesoporous solar cell consists of a FTO electrode, a dense electron transport layer, a mesoporous oxide layer, a perovskite layer, a hole transport layer, and an electrode layer. TiO_2 is the most typical mesoporous framework material, which allows the perovskite nanocrystals to penetrate into the pores of mesoporous TiO_2 by solution spin-coating and forms an interconnected absorbing layer. In this structure, TiO_2 not only plays a supporting role but also has significant functional roles, such as transporting electrons, blocking holes, and inhibiting the recombination of the electron-hole pairs in the FTO conductive substrate, which contributes to improving the photoelectric conversion efficiency of the device."

Plane Heterostructures. The typical planar heterojunction structure of the perovskite solar cells is shown in Figure 4(b). The main difference from the mesoscopic structure is that the planar structure removes the porous metal oxide framework. Two interfaces are formed between the perovskite materials and the two layers (the electron transport layer and the hole transport layer). Therefore, the electron hole pairs are separated rapidly and effectively by the electron transport layer and hole transport layer, respectively. The studies on perovskite solar cells with a planar heterojunction structure contribute to the understanding of the mechanisms of light absorption and electron-hole separation and enhance the flexibility of device optimization for the development of highly efficient laminated perovskite solar cells. Snaith's group reported a

FTO/TiO_2/$MAPbI_2Cl$/spiro-OMeTAD/Ag planar heterojunction structure of perovskite solar cells and reached a PCE of 1.8% (Qui et al., 2013). Thereafter, the group prepared a series of solar cells with the planar structure, which achieved a maximum PCE of 15.7%, a V_{oc} of 1.03 V and a FF of 0.749 under optimized process conditions (Liu et al., 2014; Liu et al., 2013). Zhou et al. (2014) realized higher electron mobility by using yttrium-doped TiO2 as the electron transport material and modified the ITO to reduce the working function, which is favoured to inject the electrons from TiO_2 to the ITO electrode. The open-circuit voltage and short-circuit current of the device were greatly improved and the PCE was as high as 19.3%. Malinkiewicz et al. (2014) prepared $MAPbI_3$ perovskite solar cells by using poly(3,4-ethylenedioxythiophene): polystyrene sulfonate (PEDOT: PSS) to replace the conventional dense TiO_2 film and achieved a PCE of 12%. This kind of structure is an inverted planar heterostructure and has the potential for preparing flexible perovskite solar cells

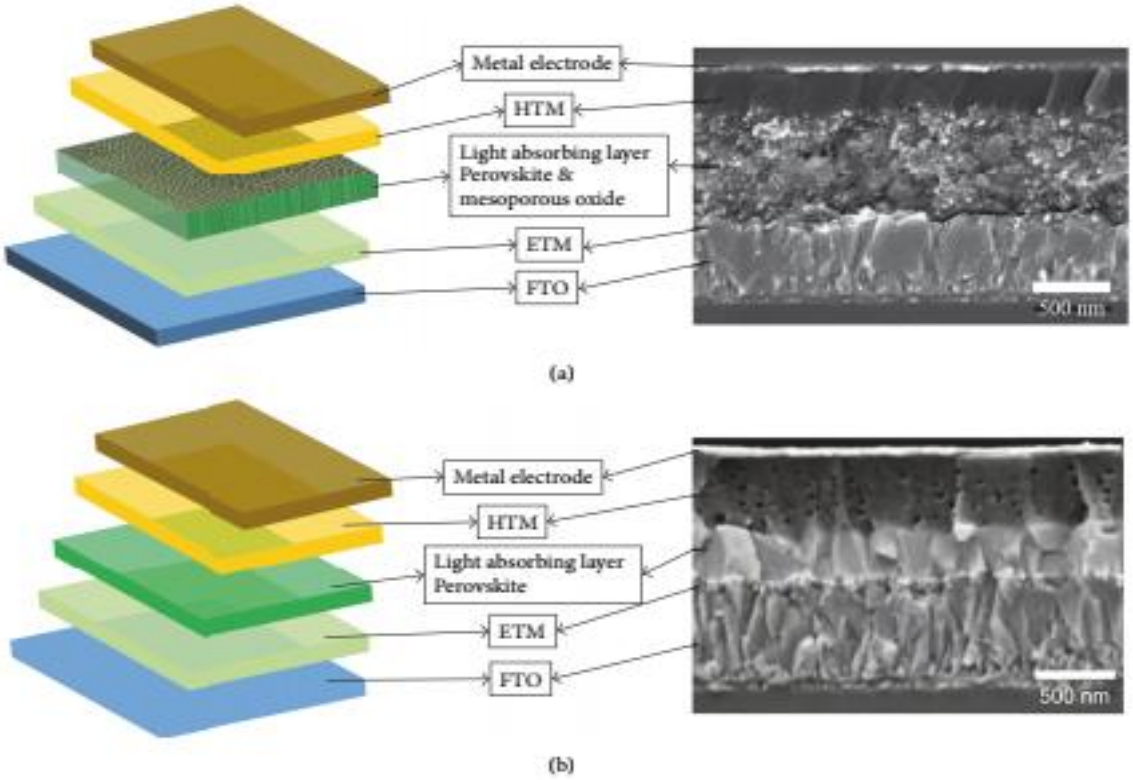

Figure 2.3: Schematic diagram and SEM section image of (a) mesoscopic architecture PSCs and (b) heterojunction structure PSCs. (Zhou et al., 2018)

2.1.3 ARCHITECTURE OF PEROVSKITE SOLAR CELLS.

There basically two types of architectures that yield high efficiency. They are the regular (n-i-p) and irregular (p-i-n). each of them can be with planer or mesoporous structure. The n-i-p mesoporous structure was the first demonstrated high-efficient structure for perovskite devices. The basic difference in structure between the n-i-p PSC in the p-i-n PSC is just the arrangement of the n-contact and p-contact in these solar cells, as shown below.

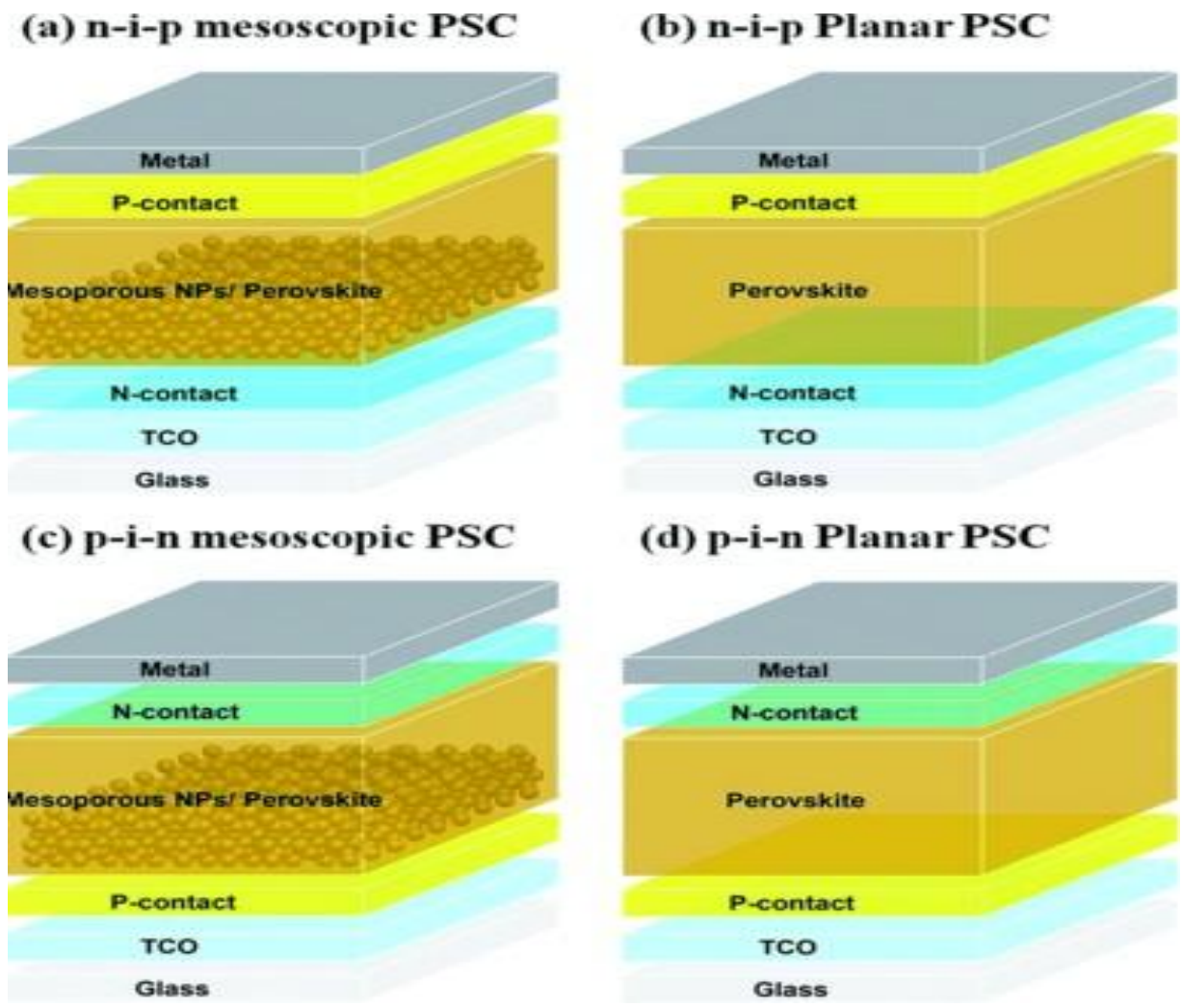

Figure 2.4: Perovskite Solar Cell Architecture (Fru Juvet, 2016)

2.1.4 STABILITY OF PEROVSKITES.

A major challenge for the advancement of the use of perovskites in replacing silicon wafers, is that although the PSCs have comparatively high PCE, it is not stable enough to be used as an alternative. This stability can be when exposed to moisture, oxygen or adverse weather conditions. It could be caused by the fabrication process of this perovskites.

Crystal Structure Stability:

Material properties are directly related to the crystal structure of materials, and their phase transition. Goldschmidt's 1927 tolerance factor describes the stability of ABX_3 perovskite materials: $t = \frac{r_A + r_o}{\sqrt{2}(r_B + r_o)}$ where, r_A, r_B and r_0 are ionic radius for organic cation A, inorganic cation B and halide anion X, respectively (Jacobsson et al., 2015) An ideal cubic perovskite structure would have a $t = 1$ and the cubic structure can only be acquired when $0.89 < t < 1$ [6]. If the tolerance factor is lower than the range, it means the symmetry will be reduced, which implies that the perovskite will shift to tetragonal or orthorhombic structure, which gives a negative effect on its opto-electronic property. (Li et al., 2017). Most stable perovskite materials have to satisfy a $0.8 < t < 1$ (Amat et al., 2014) and the most stable perovskite material is still MAPbI3, which has a tolerance factor slightly higher than 0.9 (Li et al., 2016). Other factors that can affect the phase transition of perovskite are temperature and pressure, as shown by Jain et.al, (2013) and Jiang et al., (2016) respectively.

Environmental Stability:

Moisture, high-energy photons and oxygen from the air decomposes perovskite layers during device operation. The reaction mechanism is shown below [146]. From Equations (2)–(5), with adequate moisture injected into perovskite, the MAI would be dissolved in moisture and left inorganic halide. The organic-halide would continue the hydrolysis and release HI. Since HI could be continually consumed with the assistance from oxygen and photon, the decomposition is irreversible with the existence of moisture. In addition, the perovskite itself and organic cation also tend to decompose under continuous sunlight exposure (Equations (6)–(9)). (Shi &Jayatissa, 2018)

$$CH_3NH_3PbI_3(s) \overset{H_2o}{\Longleftrightarrow} PbI_2(s) + CH_3NH_3I\ (aq.) \quad (2)$$

$$CH_3NH_3I(aq.), \Leftrightarrow CH_3NH_2(aq.) + HI\ (aq.) \quad (3)$$

$$4HI\ (aq.) + O_2 \Leftrightarrow 2I_2(s) + 2H_2O(l) \quad (4)$$

$$2HI\ (aq.) \Leftrightarrow H_2(g) + I_2(s) \quad (5)$$

$$CH_3NH_3PbI_3(s) \overset{hy}{\Leftrightarrow} PbI_2(s) + CH_3NH_2 \uparrow + HI \uparrow \quad (6)$$

$$2I^- \Leftrightarrow I_2 + 2e^- \quad (7)$$

$$3CH_3NH_3^+ \overset{hy}{\Leftrightarrow} 3CH_3NH_2 \uparrow + 3H^+ \uparrow \quad (8)$$

$$I^- + I_2 + 3H^+ + 2e^- \Leftrightarrow 3HI \uparrow \quad (9)$$

2.2 NANO-INDENTATION TECHNIQUE

Nano-indentation is a non-destructive technique which is used for the characterization of mechanical response of materials. It makes indents of nano sizes less than 200 nm (based on ISO 14577-1). It is also used majorly for thin films, as conventional mechanical and tribological testing techniques, like tensile test do not give clearly picture of the mechanical and tribological properties of thin films. Furthermore, using nanoindentation produces characterization results without any damage or delamination from substrate. It can also be used to characterize bulk materials. The mechanical properties that are usually obtained from this technique include hardness, yield strength, strain hardening coefficient, fracture toughness and viscoelastic properties of bulk materials. (Quasmi et al., 2004)

2.2.1 MEASUREMENT METHOD:

Using this technique, a load is applied on the specimen to be measure and the resultant displacement is recorded. This recoding is done continually by sensors and actuators with high resolution record penetrating depth for minute increase in load. Typical materials used as indenters include diamond, tungsten carbide, and sapphire\. Some commonly used indenter geometries are pyramidal with square base (Vickers), pyramidal with triangular base (Berkovich and cube corner), spherical and cylindrical. These are shown in figure 2.7 below.

Either the force or displacement of the indenter is usually controlled during the testing cycle. This testing cycle basically consists of linear loading to a maximum force, for a particular time, say 30 s, a hold at the maximum force for the fixed time, say 30 seconds, which allows time-dependent plasticity or creep effects to diminish, then an unloading at a set time. Although the timing is dependent on the material and the intended research, it should be choses such that the unloading curve is not significantly influenced by the creep of the material. To minimize the effect of creep and thermal drift on the unloading curve, the unloading rate is typically higher than the loading rate (Lucca et al., 2010). This results in the load displacement graph as shown in figure 2.5 below.

Table 2.1: Types of Indenters and applications.

Indenter Geometry	**Details**	**Application**
Pyramidal	Vickers type indenter with square base and angle of 136° between the opposite faces of	Used to measure mechanical properties like hardness, internal friction, strain rate sensititvity for hard materials (Ebenstein and Pruite, 2006)

	the pyramid. Berkovich type indenter with triangular base and an angle of 65.03^{o} between the axis of the pyramid	
Spherical	Different sizes ranging from 200μm to 1μm	Used for soft materials like plastic and polymers. Can also help explore yielding and associated phenomenon because the load changes gradually from elastic to plastic region.
Cylindrical	Flat tip indenter	It is rarelt used and has the advantage over other shapes in maintaining constant contact area. (Hu et al., 2015)

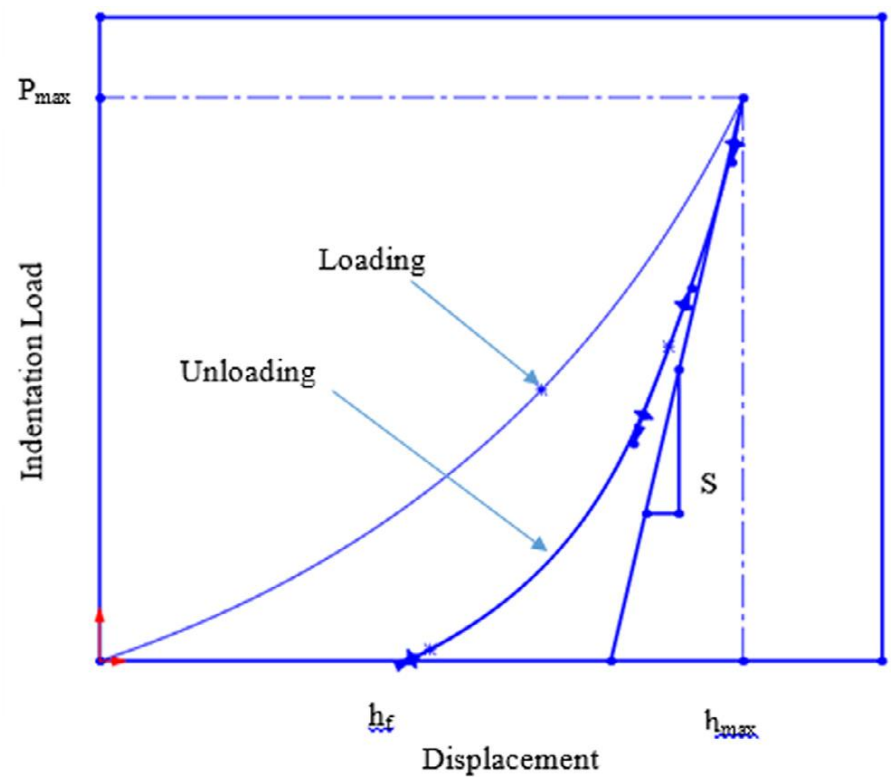

Fig. 2.5 A typical load displacement graph. (Alaboodi & Hussain, 2019)

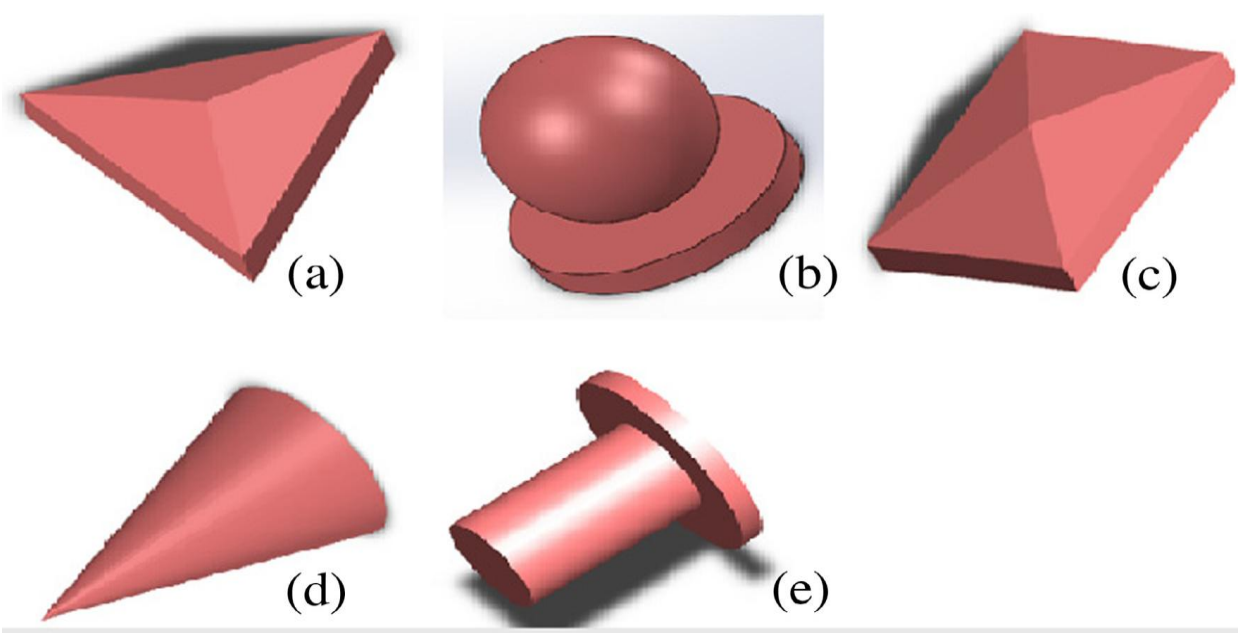

Figure 2.6: Indenter types: (a) Pyramidal Berkovich, (b) Spherical (c) Pyramidal Rockwell (d) Conical (e) Spherical (Alaboodi & Hussain, 2019)

2.2.2 ANALYSIS OF DATA

The foundation of the analysis of instrumented indentation data is on the foundation of elastic contact theory of Hertz. The works of Oliver and Pharr (14) and Field and Swain (13) have majorly been in recent times. The Oliver and Pharr (1992) method is the most widely used method for evaluating the hardness and elastic modulus. Mechanical properties are determined by calculating contact area as a function of contact depth, h_c. The area of contact is determined from the knowledge of the indenter geometry and the contact depth through the area function of the indenter. As shown in Table 2.1, indenter shape and geometry play significant role in determining the contact death. From Figure 3.5, key parameters used to calculate the contact depth are maximum load P_{max}, maximum indentation depth h_{max}, which corresponds to the maximum load and initial unloading contact stiffness "S", which is determined as the slope of the upper portion of the unloading curve during initial stages of unloading (dP/dh)

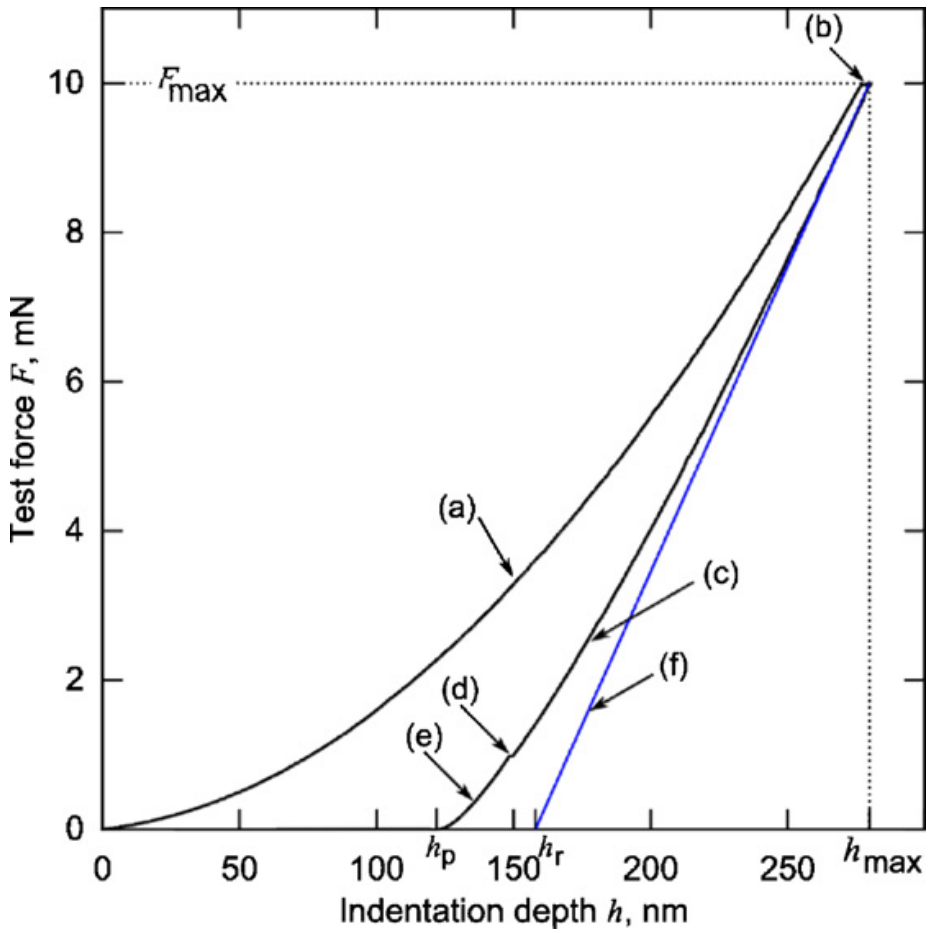

Figure 2.7: Test force vs. indentation depth plot (Lucca et al., 2010

From figure 2.7 above, the intercept of the depth axis by the tangent line to the unloading curve determines the depth h_r.

Contact depth is calculated as:

$$h_c = h_{max} - \varepsilon(h_{max} - h_r)$$

Where ε is 0,75 for a Berkovich or Vickers indenter.

The indentation hardness if given by:

$$H_{\Pi} = \frac{F_{max}}{A_p(h_c)}$$

Where F_{max} is the maximum test force and $A_p(h_c)$ is the projected area of contact of the indenter evaluated at a depth of h_c.

The Reduced Modulus calculated as:

$$E_r = \frac{\sqrt{\pi}S}{2\sqrt{Ac}}$$

Indentation modulus is given by:

$$From\ E_r = \left(\frac{(1 - {v_s}^2)}{E_s} - \frac{(1 - {v_i}^2)}{E_i} \right)^{-1}$$

$$E_{\Pi} = \frac{1 - {v_s}^2}{\frac{1}{E_r} - \frac{(1 - {v_i}^2)}{E_i}}$$

Where v_i is the Poisson's ratio of the indenter; v_s is the Poisson's ratio of the test piece; E_r is the reduced modulus of indentation contact; E_i is the elastic modulus of the indenter and S is the stiffness of the piece.

2.3 FINITE ELEMENT METHOD

The finite-element method (FEM) is quite a powerful technique used in modelling and solving elastic-plastic contact problems, which can also be used to simulated nanoindentation test. A benefit of FEM-models is its ability to analyse the loading and unloading material response to different stresses. In cases of thin film surfaces, it is even more applicable as nanoindentation experiment may not always give the exact result depending on the nature of the substrate or thin film. It can also analyse the distribution of stress and strain field, as well as profile of indentation print, as shown in Figure 2.8. More importantly also, numerical simulation comes in very handy in back analysis of nanoindentation testing data which makes it possible to obtain the material

model parameters in cases where experiments are difficult to conduct. For thin films, estimation of constitutive parameters cannot be done my beans of semi-empirical formulae. Rather, inverse modelling of nanoindentation testing, based on finite element simulation is the only feasible method. (Iankov et al., 2013).

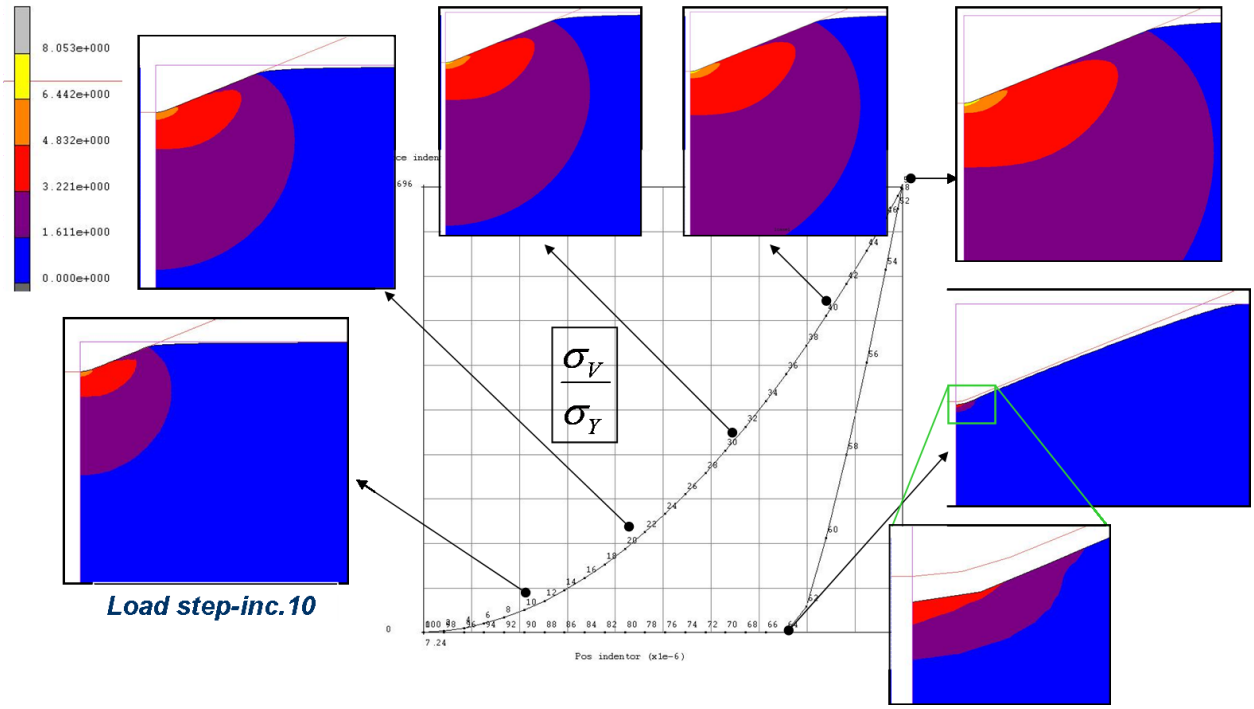

Fig 2.8. Distribution during indentation of equivalent von Mises stress normalised with respect to one dimensional yield stress (Iankov et al, 2013)

Even though the numerical model of nanoindentation is build depending on the indenter geometry and material isotropy, which leads to formation of the problem in 3D space, in the case of isotropic materials, the indenter geometry can be introduced by an equivalent conical form whose geometric characteristics have conventional indenter tips. This helps reduce more complex 3D models into axisymmetric ones that can be solved as a 2D problem thereby simplifying the numerical analysis and accelerating the process of nanoindentation back analysis procedure. (Qin et al., 2009).

The computational procedure for the elastic-plastic analysis makes use of the total Lagrangian approach, where we use small strain elasto-plasticity (the discrete equations are formulated with respected to the reference configuration t=0), mean normal return mapping and additive decomposition of strain rates. For the total Lagrangian approach, the equilibrium can be expressed by the principle of virtual work as:

$$\int_{V_o} S_{ij}\delta E_{ij} dV = \int_{V_o} b_i^o \delta\eta_i dV + \int_{V_o} t_i^o \delta\eta_i dV$$

Here S_{ij} is the symmetric second Piola-Kirchhoff stress tensor, E_{ij}, is the Green-Lagrange strain, b_i^o is the body force in the reference configuration, t_i^o is the traction vector in the reference configuration, and η_i is the virtual displacements. For small strain analysis, the material law is formulated in true Cauchy stresses, $\boldsymbol{\sigma}$, and true strains, $\boldsymbol{\varepsilon}$, and in incremental form it reads:

$$d\boldsymbol{\sigma} = \boldsymbol{L}^{ep} : d\boldsymbol{\varepsilon}, \boldsymbol{L}^{ep} = \boldsymbol{C} - \frac{(\boldsymbol{C}:\boldsymbol{\nabla}\overline{\boldsymbol{\sigma}}) \otimes (\boldsymbol{C}:\boldsymbol{\nabla}\overline{\boldsymbol{\sigma}})}{\boldsymbol{H} + \overline{\boldsymbol{\sigma}} : \boldsymbol{C} : \overline{\boldsymbol{\sigma}}}$$

Here **C** is the elastic stiffness matrix, H is the hardening coefficient, $\overline{\boldsymbol{\sigma}}$ is the von Mises equivalent stress. The elastic stiffness and the hardening coefficient for the substrate and the fil are introduced according to the assumed elasto-plastic models.

2.4 REVIEW OF PREVIOUS WORK DONE ON FEM NANOINDENTATION

Gan and Ben-Nissan (1997) while studying the effects of mechanical properties of thin film on nano-indentation data using FEA, utilized a two-dimensional axis-symmetric model to investigate the effects of elastic modulus, yield strength and strain hardening on thin films of variable thickness, saw that the yield strength and strain hardening of film have greater impact on load displacement curve whereas elastic modulus of film has negligible impact. While

calculating critical stresses for onset plastic deformation in coating and substrate failure, Michler and Blank (2001) utilised Finite Element Simulation and analysis of simulation of contact using a spherical diamond indenter on steel substrate to show that fracture load varied with height of indentation to indenter radius (h/R) ratio. Ranjana et al., (2002), in their study of the effects of substrate on the determination of thin film mechanical properties by nanoindentation saw that effect was negligible in the case of soft film on hard substrate, that effect was prominent in case of hard film of relatively soft substrate and the plastic properties (yield strength and strain exponent) of thin film is relatively superior to those of the same material in bulk. He and Veprek (2003) performed finite element analysis of super hard coatings on relatively soft materials by treating the indenter as elastic, rather than rigid, because they were working on super hard coatings, in which case indenters usually experience deformation. From their work, they discovered that Oliver-Pharr and the Doerner-Nik methods gave different hardness values when applied to load-displacement curves from a super hard film on a soft substrate. The effect of substrate was found to be quite intense in the case of super hard coating and it was recommended that indentation experiment should be performed withing 5% of coating thickness, rather than 10%. Park and Pharr (2004) carried out nanoindentation with spherical indenters to study FEA of deformation in the elastic-plastic transition regime. They took advantage of the spherical indenter, and plotted the constraint factor P_m/σ_r against a/R in order to explore the elastic plastic transition for a variety of materials, where P_m is the mean pressure under indenter, σ_r is the flow stress calculated from representative strain $\varepsilon_r = 0.2$ a/R for spherical indenter, and a and R are radius of indentation and indenter respectively. The result of Park and Pharr (2004) showed outstanding results that the elastic-plastic transition could be divided in to two regions: the elastic dominated regime, in which a single universal law holds, which could be used to estimate

material properties without prior knowledge of work hardening and the plastically dominated regime where deformation is dependent on strain hardening characteristic of material. Toparli and Koksal (2005) were able to use simulate nano-indentation test to calculate hardness and yield strength of dentin, seeing that it was difficult to measure conventionaly. Bressan et al (2005) modelled nanoindentation of bulk and thin film by finite element method to investigate the response of thing films and bulk materials of copper, titanium and iron. The effects of simulation parameters like friction, mesh size, indenter tip radius and hardening law imposed on materials was explored, which showed that thin layers on substrate show relatively good strength as compared when they are used in bulk. Beegan and Chowdhury (2004) studied the nanoindentation behaviour of hard and soft copper nitride and copper films of thickness 550 and 400nm on silicon substrates. They observed the effect of substrate. True hardness value from the measure composite was gotten by applying Korsunksy's composite harness model. Yoo et al., (2004) studied the effect of work hardening on the critical indentation limit in spherical nanoindentation of thin film substrate system. In the study, he performed finite element analysis for layered and hypothetically monolithic materials and compared the results. Making use of 2-D axis-symmetric model with spherical indenter of different radii, the critical limit was also investigated by the extent of indentation by which layered system and monolithic material show the same behaviour. The study showed initiation of equivalent plastic strain in substrate for critical indentation depth determination.

Strinivas and Eswara (2009) simulated finite element modelling of nanoindentation to extract load-displacement characteristic of bulk materials and thin films. Good agreement was found between experimental and simulated data. The author also established that nanoindentation simulation could be performed on ANSYS. Zhao et al (2011) performed nanoindentation of hard

multilayer coatings using finite element modelling. This was done in order to investigate stress distribution in four different coating systems under nanoindentations and under same conditions. There were two monolithic (single layer, pure TiN on steel and pure TiSiN on steel) systems, while the other two were multi-layered (combination TiN and TiSiN) systems. The overall thickness in all systems were constant ($2\mu m$). The comparison revelaed that there is a reduction in stress intensity in multi-layered structure. A maximum reduction of 50% in radial tensile stress was observed at interface in case of multi layered structure. Liu et al. (2013) worked on an architectural design of diamond-like carbon coatings for long-lasting joint replacements. Modulus graded multilayer structure for DLC coating used in artificial joints was analysed. The simulation was carried out in COSMOL to investigate wear particles induced stress in coatings on metal on metal (MoM) bearing hip replacement. They further analysed three types of DLC coatings (on three and five layers) were analysed. For multilayer coatings gradient in modulus is applied. 2-D axis symmetric model was simulated using spherical indenter. The results showed stress distribution mapped under the action of wear particles. Also, lowering of stress concentration, observed in multilayer coatings, justified their implementation. There was also a reduction in tensile stress, which improve crack resistance and reduction in shear stress which curtail the risk of delamination. Uysal (2015) performed computational analysis by doing a numerical modelling of functional graded TiB coating in nanoindentation on determination of mechanical properties. Tungsten Carbide (WC) and Titaniumm Boron (TiB) were used (each separately) as functional graded materials whose mechanical properties vary linearly along the thickness. The results were compared with thin coating layer of 85% Ti and 15% TiB. FGM was proved better in terms of mechanical properties because a 10% decrease in distribution, 3 times

decrease in maximum normal stress and 2 times decrease maximum shear stress were observed. Thus, the possibility of delamination would be curtailed.

2.5 REFERENCES

Alaboodi, A. S., & Hussain, Z. (2019). Finite element modeling of nano-indentation technique to characterize thin film coatings. *Journal of King Saud University - Engineering Sciences*, *31*(1), 61–69. https://doi.org/10.1016/j.jksues.2017.02.001

Amat, A.; Mosconi, E.; Ronca, E.; Quarti, C.; Umari, P.; Nazeeruddin, M.K.; Gratzel, M.; De Angelis, F. Cation-induced band-gap tuning in organohalide perovskites: Interplay of spin–orbit coupling and octahedra tilting. *Nano Lett.* **2014**, *14*, 3608–3616.

Donne, A. Le, Scaccabarozzi, A., Tombolato, S., Binetti, S., Acciarri, M., & Abbotto, A. (2013). Solar Photovoltaics: A Review. *Reviews in Advanced Sciences and Engineering*, *2*(3), 170–178. https://doi.org/10.1166/rase.2013.1030

Gan, L., Ben-Nissan, B., 1997. Comp. Mater. Sci. 8, 273–281

Iankov, R., Datcheva, M., Cherneva, S., & Stoychev, D. (2013). Finite element simulation of nanoindentation process. *Lecture Notes in Computer Science (Including Subseries Lecture Notes in Artificial Intelligence and Lecture Notes in Bioinformatics)*, *8236 LNCS*, 319–326. https://doi.org/10.1007/978-3-642-41515-9_35

ISO 14577: , Instrumented indentation test for hardness and materials parameters

Jacobsson, T.J.; Pazoki, M.; Hagfeldt, A.; Edvinsson, T. Goldschmidt's rules and strontium replacement in lead halogen PSCs: Theory and preliminary experiments on CH3NH3SrI3. *J. Phys. Chem. C* **2015**, *119*, 25673–25683

Jiang, S.; Fang, Y.; Li, R.; Xiao, H.; Crowley, J.; Wang, C.; White, T.J.; Goddard, W.A.; Wang,

Jain, A.; Castelli, I.E.; Hautier, G.; Bailey, D.H.; Jacobson, K.W. Performance of genetic algorithms in search for water splitting perovskites. *J. Mater. Sci.* **2013**, *48*, 6519–6534

Li, W.; Wang, Z.; Deschler, F.; Gao, S.; Friend, R.H.; Cheetham, A.K. Chemically diverse and multifunctional hybrid organic-inorganic perovskites. *Nat. Rev. Mater.* **2017**, *2*, 16099.

Li, Z.; Yang, M.; Park, J.S.; Wei, S.H.; Berry, J.J.; Zhu, K. Stabilizing perovskite structures by tuning tolerance factor: Formation of formamidinium and cesium lead iodide solid-state alloys. *Chem. Mater.* **2016**, *28*, 284–292

Lucca, D. A., Herrmann, K., & Klopfstein, M. J. (2010). *CIRP Annals - Manufacturing Technology Nanoindentation : Measuring methods and applications*. *59*, 803–819. https://doi.org/10.1016/j.cirp.2010.05.009

Michler, J., Blank, E., 2001. Thin Solid Films 381, 119–134

Saha, Ranjana, Nix, William D., 2002. Acta Materialia 50, 23–38.

He, J.L., Veprek, S., 2003. Surf. Coat. Technol. 163–164, 374–379.

Park, Y.J., Pharr, G.M., 2004. Thin Solid Films 447–448, 246–250.

Toparli, M., Koksal, N.S., 2005. Comput. Methods Programs Biomed. 77, 253–257

, Y.-H., Lee, W., Shin, H., 2004. Surf. Coat. Tech. 179, 324–332.

Srinivasa, Rao Ch, Eswara, Reddy C, 2009. Indian J. Pure Appl. Phys. 47, 54–59.

Qin, J., Huang, Y., Xiao, J., Hwang, K.C.: The equivalence of axisymmetric indentation model for three-dimensional indentation hardness. Journal of Materials

Research 24, 776–783 (2009)

Green, M.A.; Baillie, A.H.; Snaith, H.J. The emergence of PSCs. *Nat. Photonics* **2014**, *8*, 506–514.

Stoumpos, C.C.; Malliakas, C.D.; Kanatzidis, M.G. Semiconducting Tin and Lead Iodide perovskites with organic cations: Phase transitions, high mobilities and near-infrared photoluminescent properties. *Inorg. Chem.* **2013**, *52*, 9019–9038

Kawamura, Y.; Mashiyama, H.; Hasebe, K. Structural study on cubic–tetragonal transition of CH3NH3PbI3. *J. Phys. Soc. Jpn.* **2002**, *71*, 1694–1697.

Whitfield, P.S.; Herron, N.; Guise, W.E.; Page, K.; Cheng, Y.Q.; Milas, I.; Crawford, M.K. Structures, Phase transitions and tricritical behavior of the hybrid perovskite methyl ammonium lead iodide. *Sci. Rep.* **2016**, *6*, 35685.

Korshunova, K.; Winterfeld, L.; Beenken, W.J.D.; Runge, E. Thermodynamic stability of mixed Pb:Sn methyl-ammonium halide perovskites. *Phys. Status Solidi* **2016**, *253*, 1907–1915.

Burschka, J.; Pellet, N.; Moon, S.J.; Baker, R.H.; Gao, P.; Nazeeruddin, M.K.; Grätzel, M. Sequential deposition as a route to high-performance perovskite-sensitized solar cells. *Nature* **2013**, *499*, 316–319.

H.-S. Kim, C.-R. Lee, J.-H. Im et al., “Lead iodide perovskite sensitized all-solid-state submicron thin film mesoscopic solar
cell with efficiency exceeding 9%,” *Scientific Reports*, vol. 2, article 591, 2012

W. S. Yang, J. H. Noh, N. J. Jeon et al., “High-performance photovoltaic perovskite layers fabricated through intramolecular

exchange," *Science*, vol. 348, no. 6240, pp. 1234–1237, 2015

J. Qiu, Y. Qiu, K. Yan et al., "All-solid-state hybrid solar cells based on a new organometal halide perovskite sensitizer and one-dimensional TiO2 nanowire arrays," *Nanoscale*, vol. 5, no.8, pp. 3245–3248, 2013.

M. M. Lee, J. Teuscher, T. Miyasaka, T. N. Murakami, and H. J. Snaith, "Efficient hybrid solar cells based on mesosuperstructured organometal halide perovskites," *Science*, vol. 338, no. 6107, pp. 643–647, 2012.

J. M. Ball, M. M. Lee, A. Hey, and H. J. Snaith, "Low-temperature processed meso-superstructured to thin-film perovskite solar cells," *Energy & Environmental Science*, vol. 6, no. 6, pp. 1739–1743, 2013.

D. Bi, S.-J. Moon, L. Haggman et al., "Using a two-step deposition technique to prepare perovskite (CH3NH3PbI3) for thin film solar cells based on ZrO2 and TiO2 mesostructures," *RSC Advances*, vol. 3, no. 41, pp. 18762–18766, 2013.

S. H. Hwang, J. Roh, J. Lee, J. Ryu, J. Yun, and J. Jang, "Sizecontrolled SiO2 nanoparticles as scaffold layers in thin-film perovskite solar cells," *Journal of Materials Chemistry A*, vol. 2, no. 39, pp. 16429–16433, 2014.

D. Liu and T. L. Kelly, "Perovskite solar cells with a planar heterojunction structure prepared using room-temperature solution processing techniques," *Nature Photonics*, vol. 8, no. 2, pp. 133–138, 2014.

M. Liu, M. B. Johnston, and H. J. Snaith, “Efficient planar heterojunction perovskite solar cells by vapour deposition,”
Nature, vol. 501, no. 7467, pp. 395–398, 2013.

H. Zhou, Q. Chen, and G. Li, “Interface engineering of highly efficient perovskite solar cells,” *Science*, vol. 345, no. 6196, pp.
542–546, 2014.

O. Malinkiewicz, A. Yella, Y. H. Lee et al., “Perovskite solar cells employing organic charge-transport layers,” *Nature Photonics*, vol. 8, no. 2, pp. 128–132, 2014.

Fru Juvet, “Effect of Annealing Temperature on the Formation of Methyl-ammonium tin tri-iodide perovskite thin film”, African University of Science and Technology, online repository 2016

Zhengqi & Ahalapitaya. (2018). *Perovskites-Based Solar Cells : A Review of Recent Progress , Materials and Processing Methods*. https://doi.org/10.3390/ma11050729

Zhou, D., Zhou, T., Tian, Y., Zhu, X., & Tu, Y. (2018). *Perovskite-Based Solar Cells : Materials , Methods , and Future Perspectives*. *2018*.

Z.; Baikie, T.; et al. Pressure-dependent polymorphism and band-gap tuning of methylammonium Lead Iodide perovskite. *Angew. Chem. Int. Ed.* **2016**, *55*, 6540–6544.

W. Zhang, M. Saliba, S. D. Stranks et al., “Enhancement of perovskite-based solar cells employing core-shell metal nanoparticles,” *Nano Letters*, vol. 13, no. 9, pp. 4505–4510, 2013.

CHAPTER THREE

3.1 MATERIALS AND METHODOLOGY

For the project carried out, there was no experimental work carried out. Instead, it was mainly restricted to numerical analysis and Finite Element Modelling.

3.2 FEM TECHNIQUES EMPLOYED

The project was carried out using the commercially available Finite Element Software, ABAQUS 6.14 model. This software provides keen insight in a virtual environment to what takes place under the tip of the indenter through its analysis of the loading and unloading material response of different models. ABAQUS software further analysis the distribution of stress and strain fields as well as the profile of indentation imprint. Since the materials for the simulation are isotropic, we carried out the simulation using a 2D axisymmetric model, which accelerates the process of indentation.

3.3 SPECIFICATIONS OF MATERIALS MODEL

The model was consisting of two main parts: the sample (which included the substrate and the thin film) and the Berkovich indenter.

For the Berkovich indenter, the equivalent conical indenter has a semi-angle of 70.3^{o}, so that the ratio of cross-sectional area to depth is the same as for a Berkovich+- indenter and the cone tip rounding of R=20nm. The reason why this rounding is accounted for is because indentation tests on thin films may be with thickness less than 500 nm, which suggests very shallow indentation depths where the sharpness of the cone has influence. Since the indenter materials are made of

very hard materials, like diamond, it is modelled as a rigid body. Since the penetration size is about 600nm maximum, it should work fine. For the Berkovich Indenter, the materials chosen is diamond, with Young's modulus, 1140 GPa and Poisson's ratio of 0.07.(Pandure et al., 2014)

The FTO-coated glass substrate occupies a rectangular domain with dimensions $25\mu m \times 40\mu m$. The material model for the substrate is the elastic-plastic model with linear hardening and von Mises yield surface.

The thin film takes the upper rectangular part of the model with dimensions $25\mu m \times 2.76\mu m$. The materials response of the film is assumed to be first elastic, then elastic-plastic with properties as Young's Modulus 0.7GPa and Poisson's ratio 0.22 and a linear relationship between yield stress and plastic strain as 5 to 0 and 12 to 0.45 respectively.

The basic dimension used in the model for the FEA are mm for length and Newton for force. This gives resulting stresses the unit of MPa

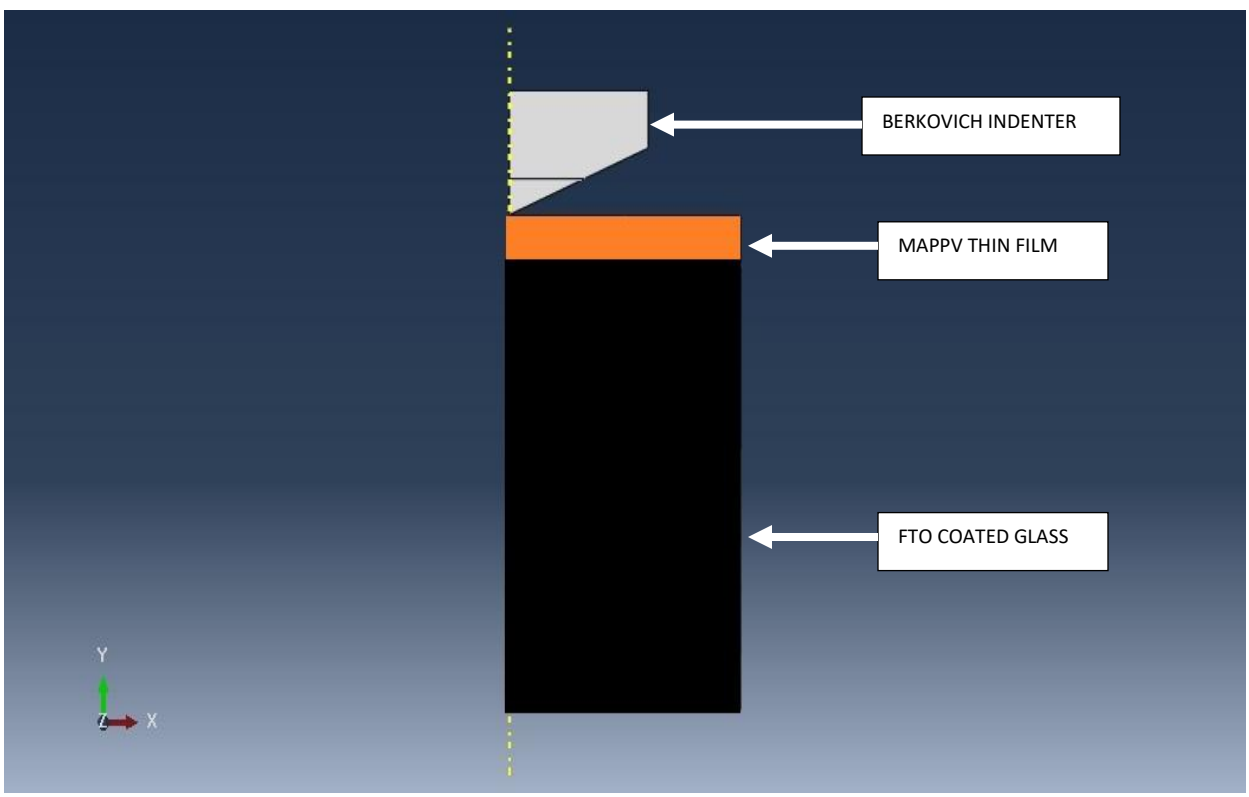

Figure 3.1 Schematic of setup for nanoindentation simulation

3.3.1 SIMULATION OF NANOINDENTATION PROCESS

We first make the following assumptions prior to the simulation:

- The indentation process is quasi-static
- There is full adhesion between the film and the substrate, the thin film and substrate are perfectly bonded and there is no delamination or slippage at the interface.
- Friction forces in the contact area are neglected. Also, the surface in the model are ideally smooth, which implies that surface roughness effects are not considered.
- No previous history of stress-strain relationship is taken into account.
- The indenter material and the specimen are both isotropic.
- The indenter tip wearing during the indentation process was neglected.

3.3.2 CONTACT PAIR AND MODELS

The indentation process of penetration, holding and retraction is simulated as a deformable-rigid contact problem via constraint procedure, as the specimen in deformable, while the indenter is rigid. The bottom of the indenter and the top of the specimen material are the areas in contact. This contact was established using (model). The basic parameters used in the simulation is setting each unit length to represent 1 mm, while the unit force is set as 1 N. This gives makes the subsequent units of stress to be in MPa. To simulate the process, this was done using a step function. The indenter is set at 1e-4 mm from the sample. To better understand the interaction that takes place at the tip of the indenter and the surface of the thin film, the set up was subdivided, so that we could make the discretization at the point of interaction finer than, say towards the bottom of the indenter as shown below:

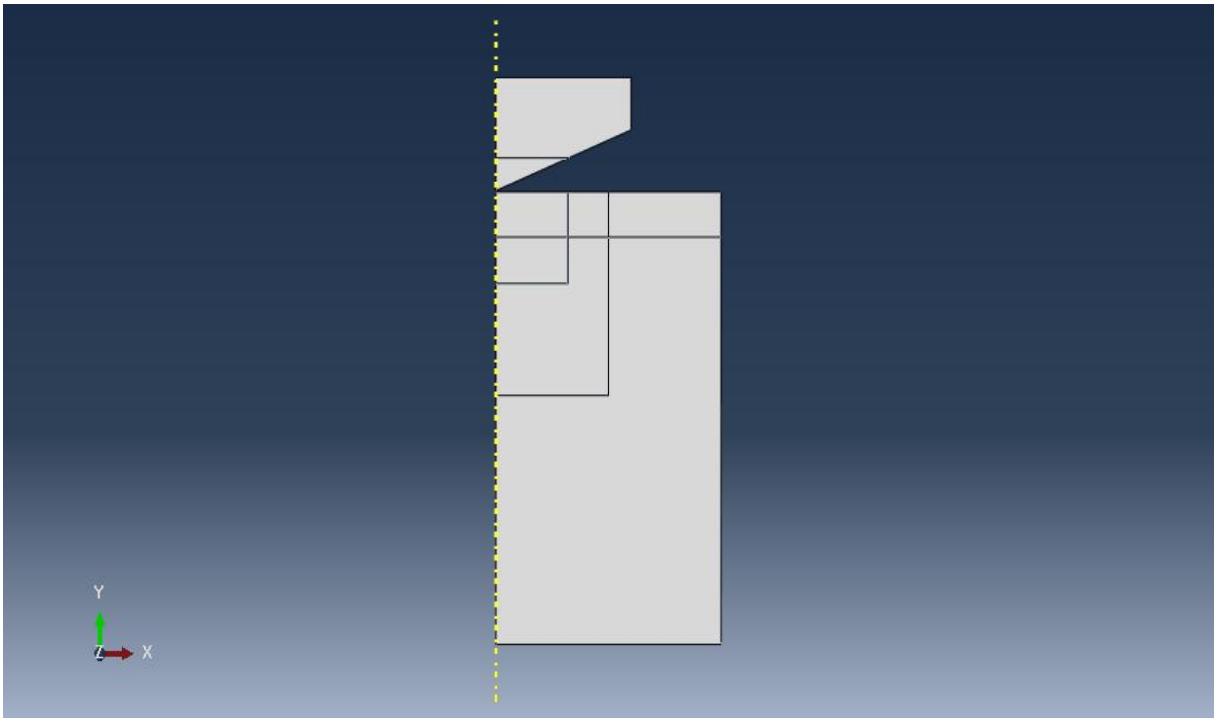

Figure 3.2: Sectioning of the set-up for finer discretization at the points of contact.

Under the property module, we create three different materials, the Berkovich indenter, the thin film MAPPV and the FTO-coated glass substrate, each of them with their mechanical properties obtained from literature. The properties are then assigned to the three basic sections of the set up.

Then Under assembly, we create instance and define a set. The allocation of sections of the sample to different sets makes it a lot easier to work with, changing specific properties and loading conditions without completely changing the whole setup fundamentally. I further assign instances to the left, right and bottom of the sample in order to specify some constraints in the

indentation process. A reference point is created where the reaction forces on the indenter are measured. The load is constrained on the reaction point.

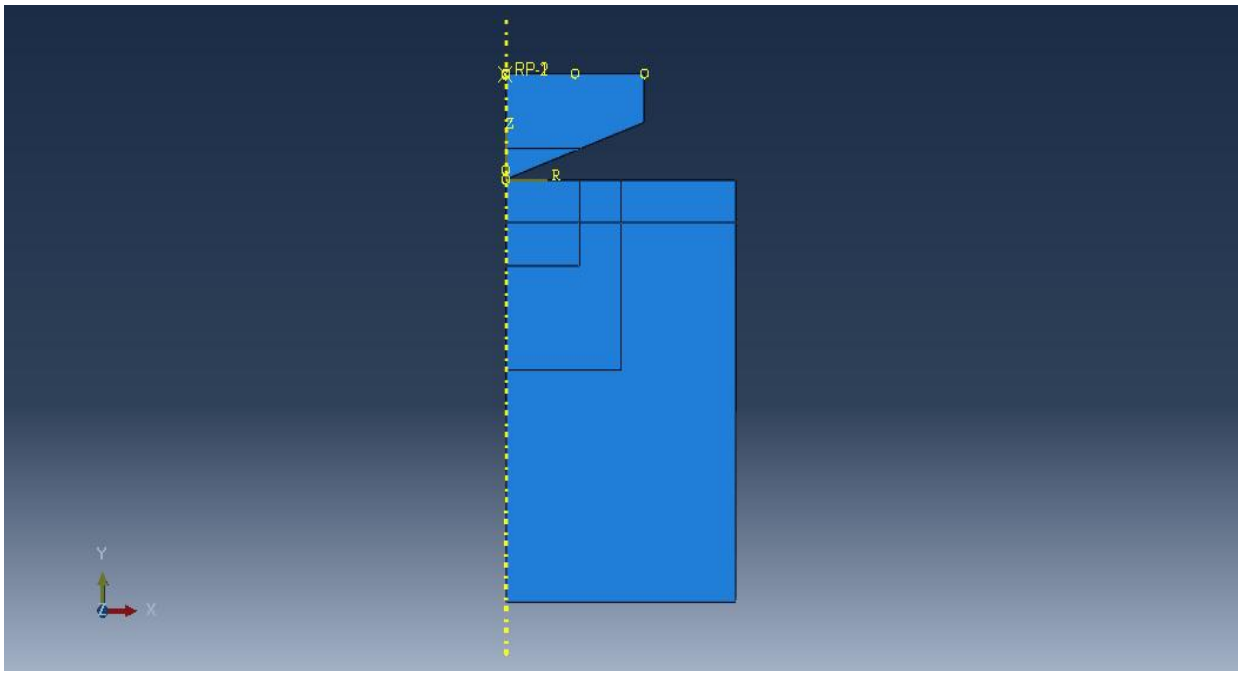

Figure 3.3: Creation of instances and reference points.

3.3.3 CONSTRAINTS AND BOUNDAERY CONDITIONS

Along the axis of symmetry, roller boundary conditions are applied. The substrate base is constrained by fixed displacements in the y-direction. The left and right side of the sample was constrained in the x-direction (restricting sidewasys movement of the sample as in normal indenter. Applied load was the displacement load which is constrained on the reaction point as -1. As such, the reaction forces are localised on that reaction point.

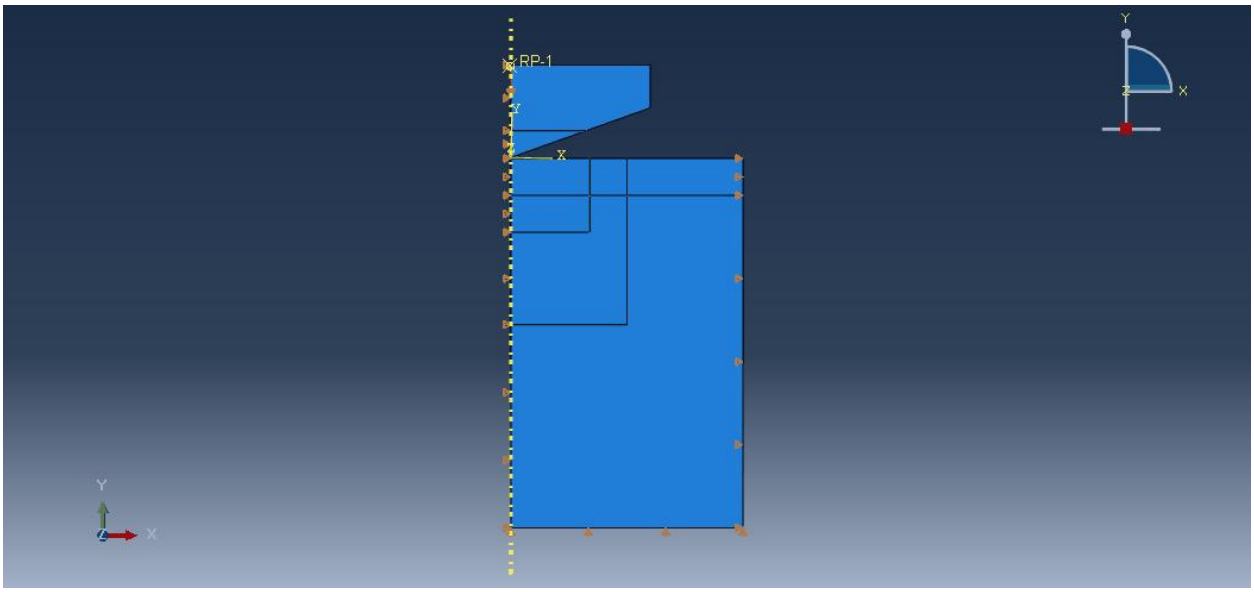

Figure 3.4 Creation of constraints on all axes of movement

3.3.4 MESHING AND DISCRETIZATION

First, a seed of 0.002 is created for the whole setup. The specimen is discretized with displacement formulated isoperimetric quadrilateral finite elements. Around the contact area, finer discretization is used. Also, the finer element mesh is done continuously coarser as it gets away from the tip. The size at the exact portion of contact is 0.0002 and it increases through the second portion until it extends to the end of the material, with coarser meshes of 0.01.

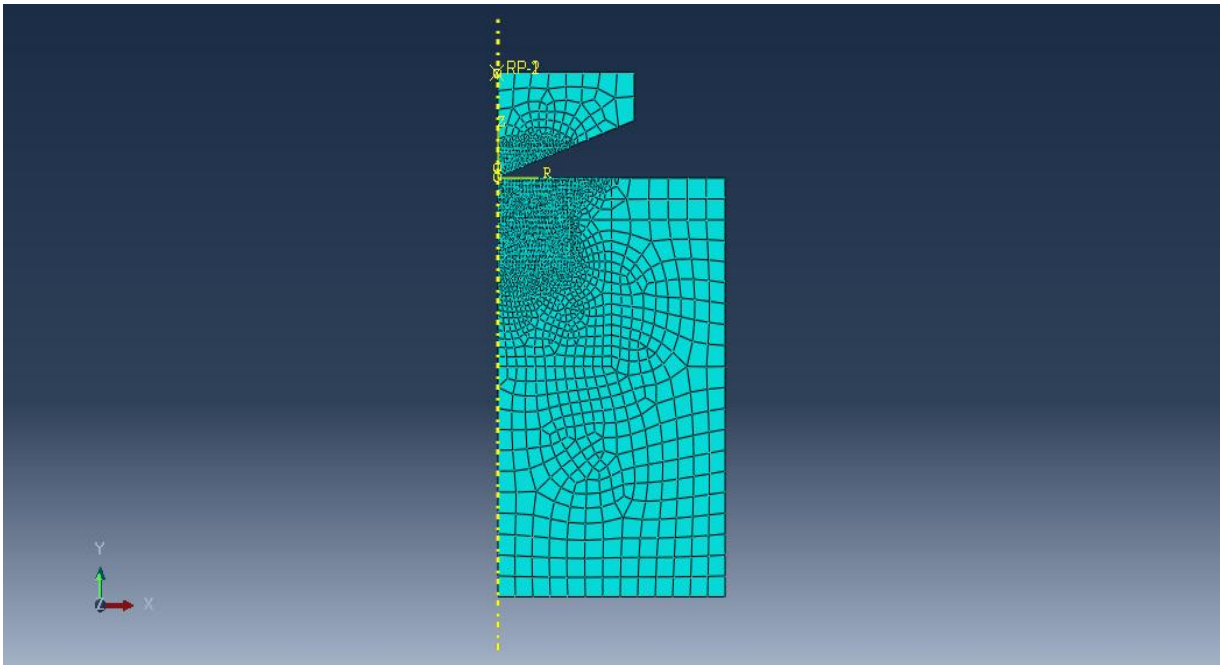

Figure 3.4: Overview of the meshed surface

After setting the meshing of the sample, we simulate nanoindentation process by setting it up thus:

Table 3.1: A table of Time and Amplitude for simulation

S/N	Time/Frequency	Amplitude
1.	0	0
2.	0.5	2e-3
3.	1	0

The simulation process then takes place with the von Misses stress distribution, Load-displacement observable from the results for both plastic and elastic-plastic films. These are further discussed in the next chapter.

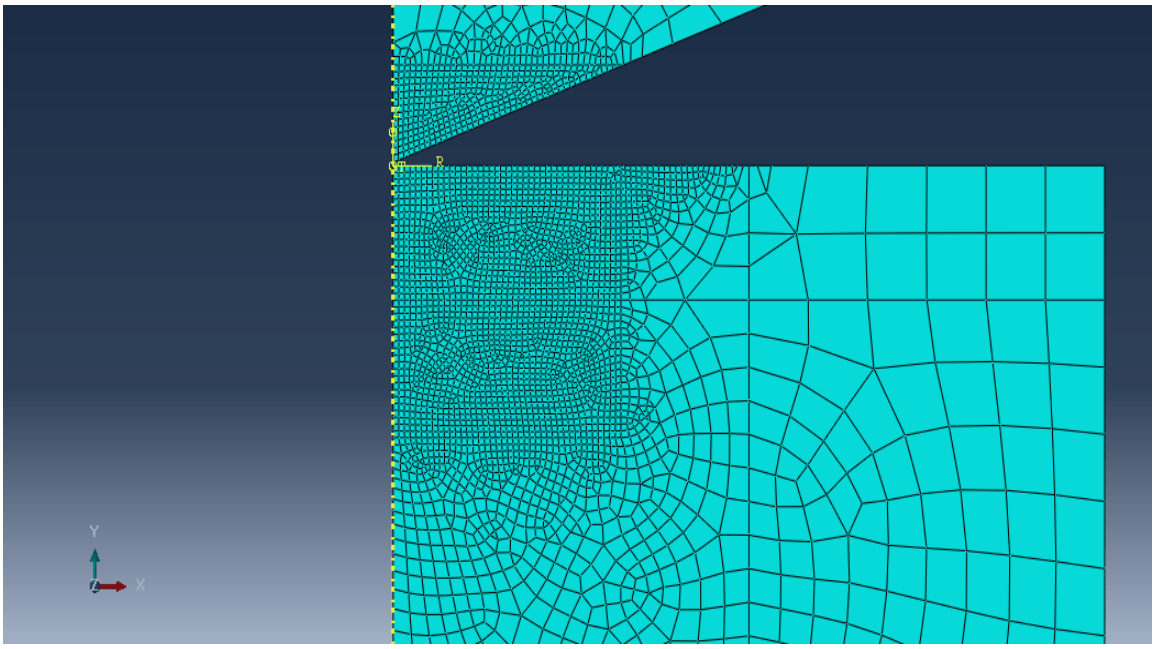

Figure 3.5: Closer view of finer meshes at the point of impact.

3.4 REFERENCES

Pandure, P. S., Jatti, V. S., & Singh, T. P. (2014). Finite Element Simulation of Nano-indentation of DLC Coated HSS Substrate. *Procedia Materials Science*, *6*(Icmpc), 1619–1624. https://doi.org/10.1016/j.mspro.2014.07.145

Pelegri, A. A., & Huang, X. (2008). Nanoindentation on soft film/hard substrate and hard film/soft substrate material systems with finite element analysis. *Composites Science and Technology*, *68*(1), 147–155. https://doi.org/10.1016/j.compscitech.2007.05.033

CHAPTER FOUR

4.0 RESULTS AND DISCUSSION

Due to the fact that the exact data on the elastic-plastic properties of MHPPV could not be obtained either from literature or experimentally, owing to a fault in the nano indenter at the laboratory, the simulation process was carried out using data of other similar materials sourced from literature, as indicated in Chapter 3.

4.1 PURELY ELASTIC THIN FILM

First, the thin film was assumed to be purely elastic, and the finite element analysis was carried out with the indentation depth of 200 nm.

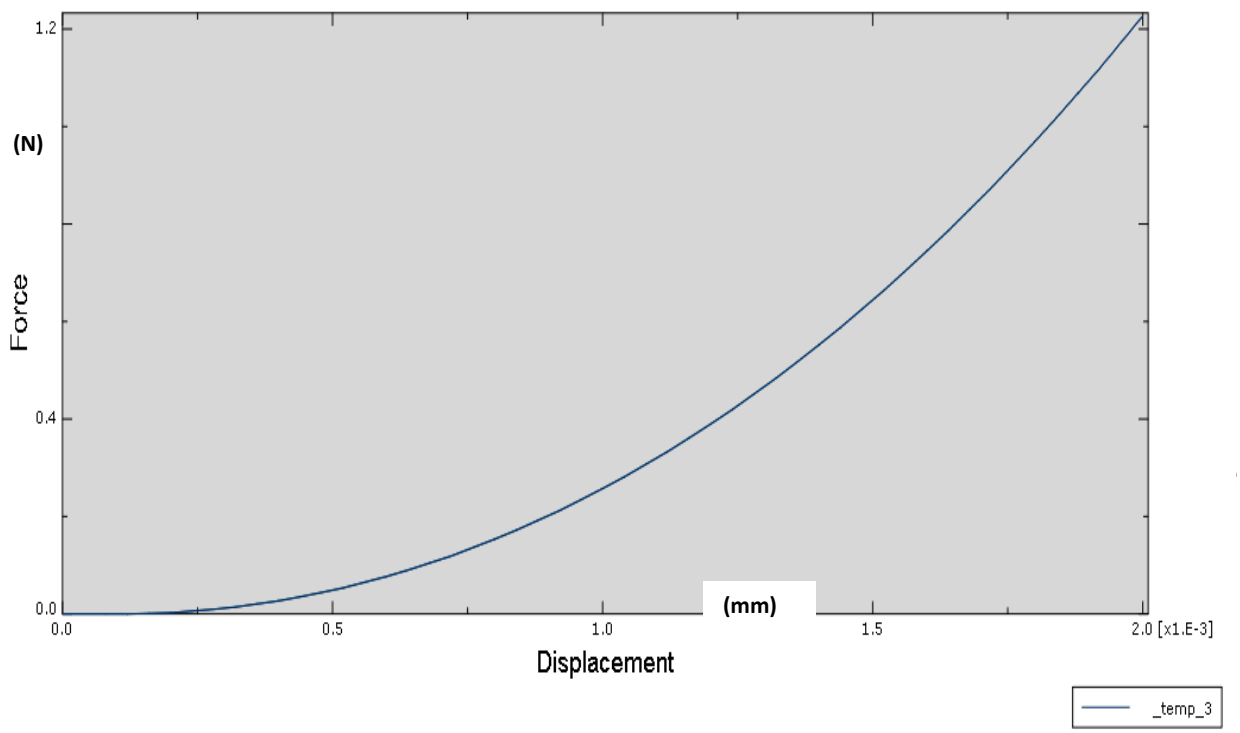

Figure 4.1: Force-displacement diagram for purely elastic thin film

For purely elastic thin film, the loading and unloading curve are continuous and coincide as the material response is the same in both cases. The maximum load observed at the maximum

indentation depth of 200 nm is 1.2 N Furthermore, upon retraction of the indenter, there is zero plasticity. This was confirmed by Poon in his doctoral thesis (Poon, 2009)

Figure 4.2. Zero plastic strain for perfectly elastic thin film

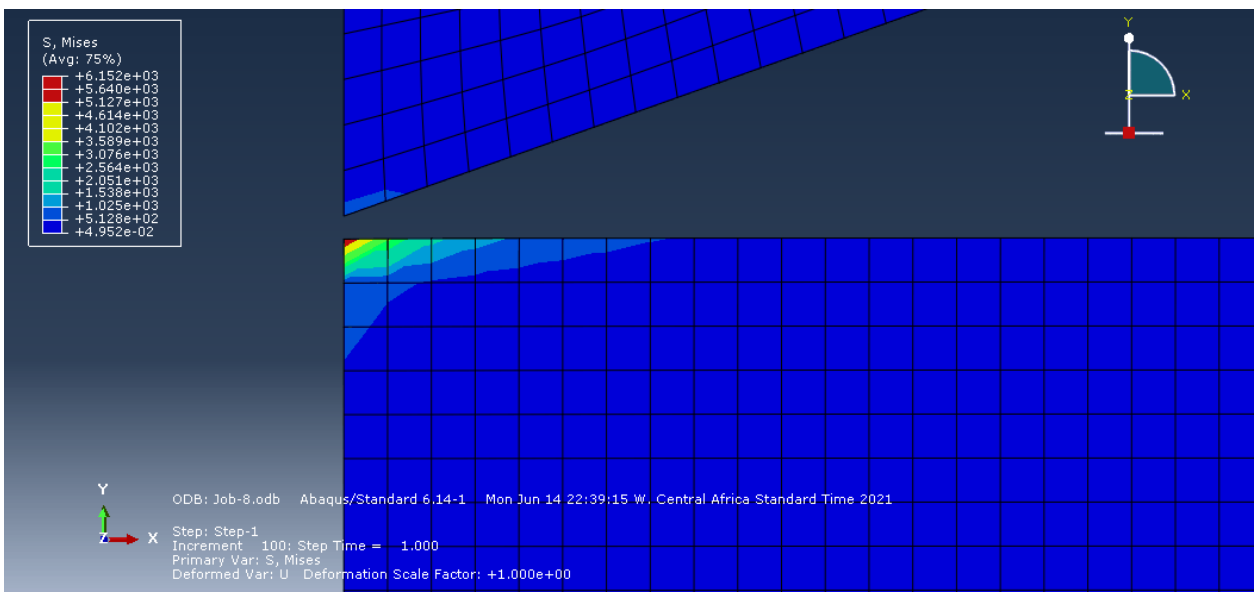

Figure 4.3 Diagram showing Mises equivalent stress distribution on the sample. Upon retraction, the material still regains its shape.

The region with highest stress is directly beneath the indenter. Mises stress progressively decreases from 6.152 KN at the tip to close to zero on the body of the substrate

4.2 ELASTIC-PLASTIC THIN FILM

For the film with both elastic and plastic properties, upon the retraction of the indenter, the shape of the deformation is seen on magnification.

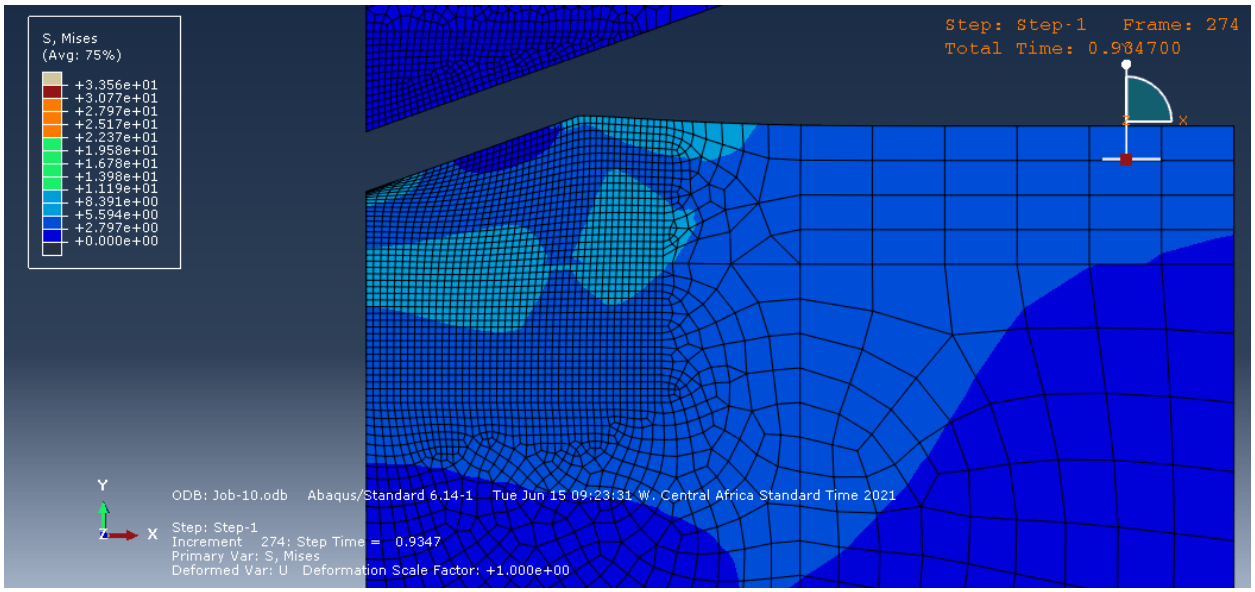

Figure 4.4. Diagram showing that the film still retains the shape of the indenter upon retraction

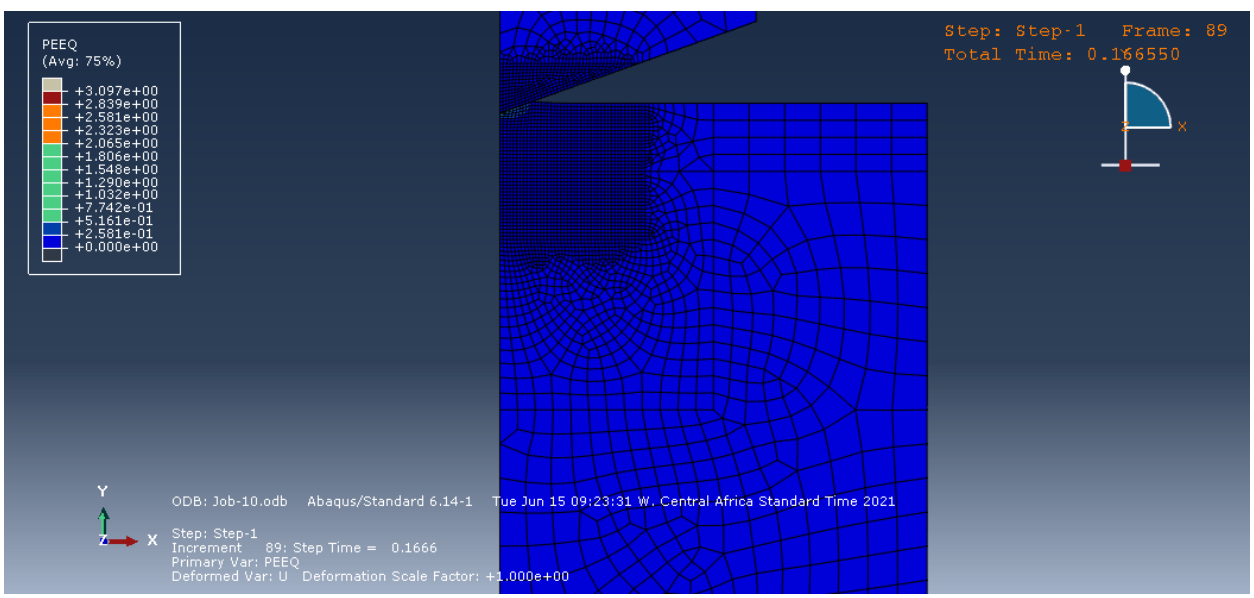

Figure 4.5 PEEQ, Plastic distribution in elasto-plastic materials.

The von Mises stress distribution for the elastic-plastic material also decreases from 3.5 to 0 Pa, which is better seen.

4.3 CALCULATION OF MATERIAL PROPERTY.

Using a rounded nanoindentation data of epoxy from the lab to do our proper analysis as follows:

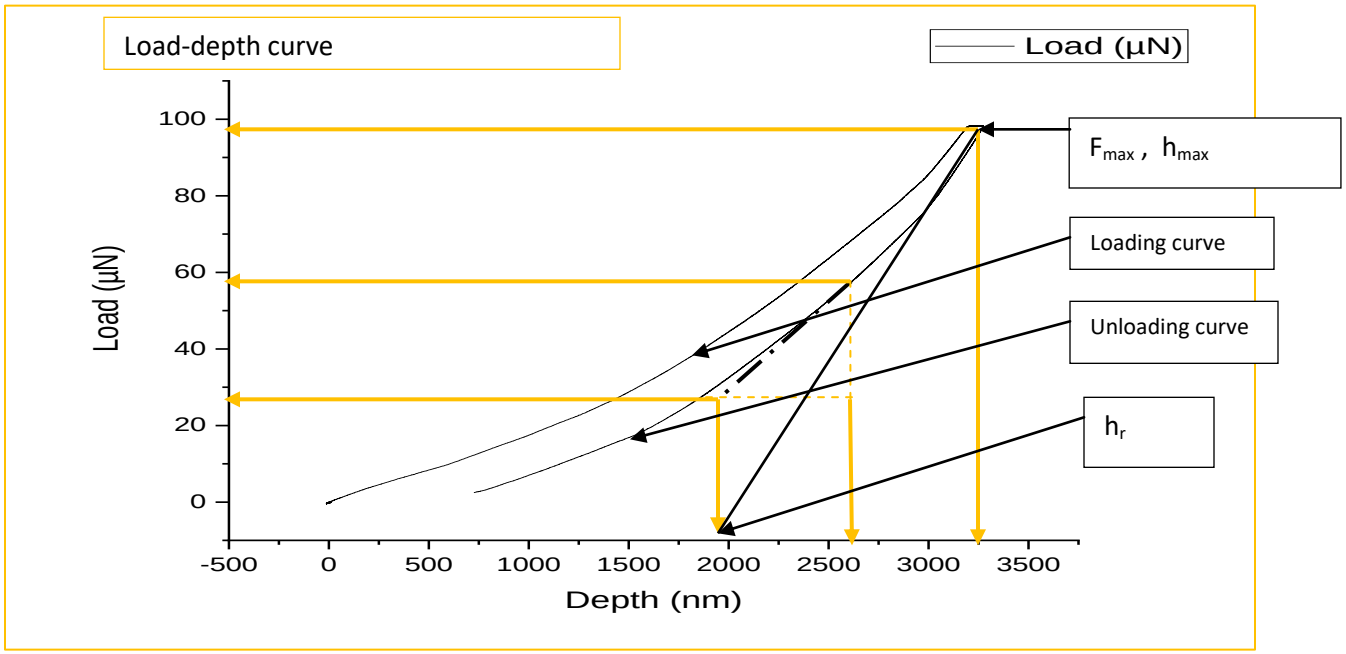

Figure 4.6: Graph showing the load displacement curve for elastic-plastic PDMS which is used

The graph above is a plot of the indentation load against indentation depth made on Origin 2019b. It basically consists of a loading, holding and unloading time. At the point of maximum load, Fmax, it corresponds to the maximum depth, h_{max}. At that point a tangent to the unloading curve is drawn, indicating where it intersects the depth axis (hr). the slope of the unloading curve is also noted with the dotted lines, and their corresponding values are traced on both the load and depth axes. It is from these key data from the graph that we extract the necessary information to obtain the mechanical properties using the Oliver and Pharr method.

Contact depth: This is different from the total indentation depth, (h) or the depth left after the removal of the indenter. The contact depth is the distance between the tip of the indenter on the

material and the exact portion where the indenter is no longer in contact with the material as shown in the figure below.

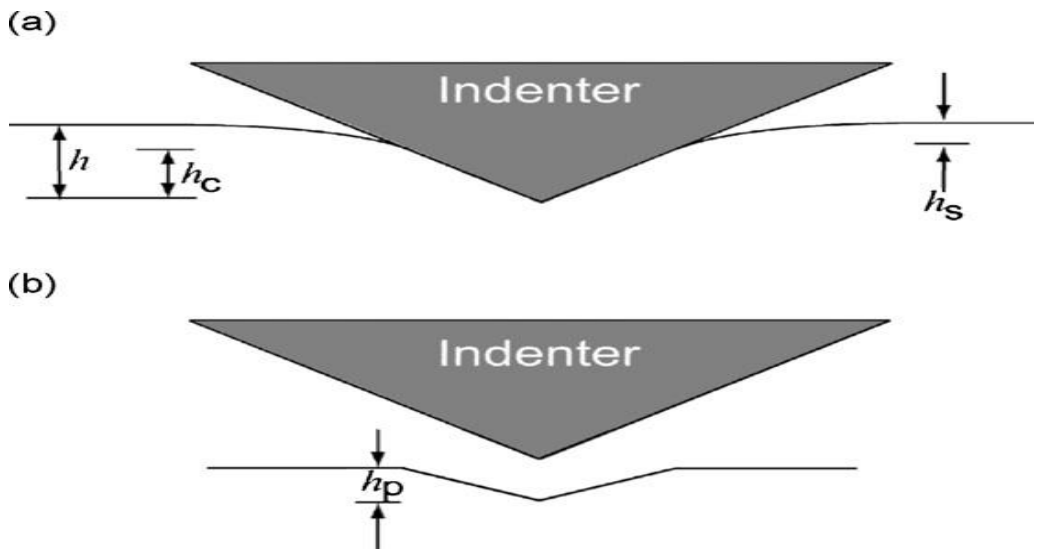

Figure 4.7 Schematic drawing of indentation surface showing (a) indenter with applied test force and (b) after removal of the test force. Indentation depth under applied test force, h, depth of contact of the indenter with the test piece h_c, depth below surface not in contact with indenter h_s and permanent indentation depth after removal of test force h_p, are denoted. (Lucca et al., 2010).

From Oliver and Pharr's method, the contact depth is calculated thus:

$$h_c = h_{max} - \varepsilon(h_{max} - h_r)$$

Where,

$$h_{max} = 3255nm, h_r = 1800nm\ (from\ Fig\ 4.7)$$

$$And\ \varepsilon = 0.75\ for\ Berkovich\ indenter,$$

$$h_c = 3255 - 0.75(3255 - 1800)$$

$$h_c = 2163.75nm.$$

Thus, the Contact depth is $2163.75nm$.

Projected Area of Contact by the indenter: From the Contact depth, we can calculate the area of contact as:

$$A_c = 24.56{h_c}^2$$

$A_c = 24.56(2163.75 \times 10^{-9})^2$

$A_c = 114.99 \times 10^{-12}\ m^2$

Hardness: The hardness is obtained by the expression:

$$H = \frac{F_{max}}{A_c}$$

$$H = \frac{98 \times 10^{-6}N}{114.99\ X\ 10^{-12}m^2}$$

$$H = 0.85\ MPa$$

Stiffness (S): This is obtained from the slope of the unloading curve as:

$$S = \frac{dP}{dh}$$

$$S = \frac{60 - 23\ (N)}{2650 - 1900\ (nm)}$$

$$S = 49.33N/m$$

Reduced Modulus(E_r): This is the reduced modulus of indentation contact and is calculate thus:

$$E_r = \frac{\sqrt{\pi}S}{2\sqrt{Ac}}$$

$$E_r = \frac{\sqrt{\pi}\ X\ 49.33}{2\sqrt{114.99\ \times 10^{-12}}}$$

$$E_r = 4.076MPa$$

Modulus of Sample(E_s): Finally, to get the indentation modulus of the material, we utilize the results obtained from the reduced modulus as:

$$From\ E_r = (\ \frac{(1 - {v_s}^2)}{E_s}\ -\ \frac{(1 - {v_i}^2)}{E_i})^{-1}$$

Where v_s is the Poisson's ratio of the sample and v_i is the Poisson's ratio of the indenter.

$$E_s = \frac{1 - {v_s}^2}{\frac{1}{E_r} - \frac{(1 - {v_i}^2)}{E_i}}$$

$$E_s = \frac{1 - 0.4^2}{\frac{1}{4.076 \times 10^6} - \frac{(1 - 0.07^2)}{1141 \times 10^9}}$$

$$E_s = 3.42\ MPa$$

4.4 REFERENCES

Lucca, D. A., Herrmann, K., & Klopfstein, M. J. (2010). *CIRP Annals - Manufacturing Technology Nanoindentation : Measuring methods and applications*. *59*, 803–819. https://doi.org/10.1016/j.cirp.2010.05.009

B. Poon, A critical appraisal of nanoindentation with application to elastic–plastic solids and soft materials, Ph.D. diss., California Institute of Technology, 2009.

CHAPTER FIVE

5.1 CONCLUSION

This work presents the result of nanoindentation through finite element analysis (FEA) on the active layer and FTO-coated glass of hybrid solar cells. The geometries of the setup used were similar to what is obtainable in different published work as indicated in Chapter 2. Also, published mechanical properties of the Berkovich indenter and the substrate, were incorporated in the simulation. They were used to study the mechanical properties of the setup.

The results obtained were consistent with those published by other authors. On using a purely elastic thin film, the force-displacement curve produced showed a merging of both the loading and unloading curves, as expected. Furthermore, for an elastic-plastic layer, the nanoindentation data gave a graph, which on using the Oliver and Pharr method, the hardness and modulus were easily calculated. Different parameters were not varied in the work, as it was intended to demonstrate whether FEA could produce accurate results for different layers of the hybrid solar-cell set up. It can therefore give further and clearer insights as to what exactly happens under the indenter.

5.2 RECOMMENDATIONS

A challenge faced was in the experimental aspect of the project in order to obtain accurate data relative to the material. I therefore suggest the following for possible future work:

1. Experimental work should be carried out to validate the results of the finite element model. This is very crucial when attempting to translate laboratory results to actual practical fabrication.

2. The simulations should also be carried out in atomic scale models, as it would facilitate better understanding of possible interactions and effects that might be overlooked in a micro-level study.
3. Other opto-electronic properties can also be examined in relation to its mechanical properties in order to get the optimal blend.
4. In carrying out subsequent simulations, parameters like indentation depth, depth of MAHPPV layer etc can also be varied to obtain a better feel of the process.
5. Finally, possible sink-in effects should be studied with finite element analysis.

in order to carry out the simulation. I recommend that for the effective study, experimental data should be used in order to validate the results obtained.

APPENDIX

A cross-section of some of the nanoindentation data points used for the elastic-plastic material response

Number of Points = 4373

Depth (nm)	Load (µN)	Time (s)	Depth (V)	Load (V)
16.235344	-0.028108	0.000000	0.000081	0.243418
16.109033	0.041084	0.085036	0.000145	0.243410….
15.976118	-0.017545	0.240102	0.000244	0.242491….
14.896262	-0.015100	0.375160	0.000503	0.240928
14.847842	-0.004070	0.380162	0.000515	0.240921….
13.922837	-0.035923	0.500213	0.000739	0.239374
13.987060	-0.045811	0.505215	0.000730	0.239375….
12.810195	-0.080507	0.630269	0.001002	0.237507
12.733177	-0.095449	0.635271	0.001018	0.237323….
11.908113	-0.038041	0.685292	0.001191	0.236575
10.858805	-0.089732	0.810345	0.001440	0.234732
…….	……	……..	……	……
…….	……	…….	……..	……..
0.000000	-0.094002	5.280870	0.005559	0.207326